Seasonal energy storage for zero-emissions multi-energy systems via underground hydrogen storage

Paolo Gabrielli [a], Alessandro Poluzzi [b], Gert Jan Kramer [c], Christopher Spiers [d], Marco Mazzotti [a], Matteo Gazzani [c,*]

[a] *Institute of Process Engineering, ETH Zurich, 8092, Zurich, Switzerland*
[b] *Department of Energy, Politecnico di Milano, Via Lambruschini 4, 20156, Milano, Italy*
[c] *Copernicus Institute of Sustainable Development, Faculty of Geosciences, Utrecht University, Princetonlaan 8a, 3584 CB, Utrecht, The Netherlands*
[d] *Department of Earth Sciences, Faculty of Geosciences, Utrecht University, Princetonlaan 8a, 3584 CB, Utrecht, The Netherlands*

ABSTRACT

The deployment of diverse energy storage technologies, with the combination of daily, weekly and seasonal storage dynamics, allows for the reduction of carbon dioxide (CO_2) emissions per unit energy provided. In particular, the production, storage and re-utilization of hydrogen starting from renewable energy has proven to be one of the most promising solutions for offsetting seasonal mismatch between energy generation and consumption. A realistic possibility for large-scale hydrogen storage, suitable for long-term storage dynamics, is presented by salt caverns. In this contribution, we provide a framework for modeling underground hydrogen storage, with a focus on salt caverns, and we evaluate its potential for reducing the CO_2 emissions within an integrated energy systems context. To this end, we develop a first-principle model, which accounts for the transport phenomena within the rock and describes the dynamics of the stored energy when injecting and withdrawing hydrogen. Then, we derive a linear reduced order model that can be used for mixed-integer linear program optimization while retaining an accurate description of the storage dynamics under a variety of operating conditions. Using this new framework, we determine the minimum-emissions design and operation of a multi-energy system with H_2 storage. Ultimately, we assess the potential of hydrogen storage for reducing CO_2 emissions when different capacities for renewable energy production and energy storage are available, mapping emissions regions on a plane defined by storage capacity and renewable generation. We extend the analysis for solar- and wind-based energy generation and for different energy demands, representing typical profiles of electrical and thermal demands, and different CO_2 emissions associated with the electric grid.

1. Introduction

The transition from fossil fuels to renewable energy sources (RES) is one of the key measures to mitigate climate change and to build a sustainable, reliable, and secure energy supply system [1,2]. Within this framework, energy storage allows to fully exploit the potential of RES by offsetting the mismatch between the fluctuating energy generation and demand, as well quantified in the early work of Schoenung [3]. Other important measures, which often offer interesting cost-opportunities, include supply and demand response, cross-sectors coupling, improved grid ancillary services, and grid infrastructure update [4,5]. Independently of their economic viability, whose analysis needs to consider the trade-off between the cost of the storage unit and the expenditure avoided by not purchasing energy from the grid, energy storage systems allow to reduce direct carbon emissions as long as renewable-based overproduction is present, and fossil generation is connected to the grid [6,7]. Indeed, the possibility of storing energy during a period of energy overproduction, and of reusing it during periods of energy shortages, removes the need of flexible fossil-based generation and the corresponding carbon emissions (Fig. 1-a). In fact, diverse storage options are necessary to deal with the variability of energy generation and demand at different time scales, ranging from hourly to seasonal. On the one hand, short-term storage technologies, e.g. batteries, feature high round-trip efficiencies but high self-discharging losses for long inactive time [8]. On the other hand, long-term storage systems, e.g. power to hydrogen (PtH$_2$), are characterized by negligible self-discharging losses

Notation

Symbols

A	cavern surface, [m^2]
a	area available for renewable generation, [m^2]
b	gas slippage factor, [Pa]
c	model constants for porosity and permeability
D	depth of the cavern, [m]
E	stored energy, [kWh]
e	annual CO_2 emissions, [ton$_{CO_2}$/yr]
F	input power, [kW]
g	gravity acceleration, [m/s^2]
H	cavern height, [m]
h	lower heating value, [kJ/kg]
I	solar irradiance, [kWh/m^2]
K	permeability constant, [1/m]
k	hydrogen permeability, [1/m]
J	total annual costs, [€/kWh]
L	energy demand, [kW]
M	molar mass, [kg/kmol]
M	number of available technologies, [−]
m	mass flow rate, [kg/s]
N	length of time horizon, [−]
n	Number of breakpoints, [−]
P	output power, [kW]
p	hydrogen pressure, [Pa]
q	single wind turbine output power [kW]
R	ideal gas constant, [kJ/(kmol K)]
r	available RES surplus, [−]
r	radial coordinate, [m]
R_i	inner radius, [m]
R_o	outer radius, [m]
S	technology size, [kW]
s	available storage capacity, [MWh$_{H_2}$/GWh$_e$]
T	temperature, [K]
t	temporal coordinate, [s]
U	imported power, [kW]
u	energy import price, [€/kWh]
V	cavern volume, [m^3]
V	exported power, [kW]
v	velocity, [m/s]
v	energy export price, [€/kWh]
W	wind velocity [m/s]
x	binary variable for on/off scheduling, [−]
x	dimensionless radial coordinate, [−]
Z	Number of wind turbines per unit area, [1/m^2]
z	hydrogen compressibility factor, [−]

Greek symbols

α	linear model constant, [−]

β	pressure ratio, [−]
Γ	characteristic capacity, [−]
γ	linear model constant, [−]
δ	fraction of geostatic pressure, [−]
ϵ	carrier emission rate, [g$_{CO_2}$/kWh]
ϵ	dimensionless porosity, [−]
ζ	linear model variable (square pressure) [Pa^2]
η	parameters of compressor linear model, [−]
κ	dimensionless permeability, [−]
Λ	annual electricity demand, [kWh]
μ	viscosity, [Pa m]
Π	dimensionless cavern pressure, [−]
π	dimensionless rock pressure, [−]
ρ	density, [kg/m^3]
$\widehat{\rho}$	density per unit pressure, [kg/(m^3 Pa)]
τ	dimensionless temporal coordinate, [−]
φ	rock porosity, [−]
ξ	specific renewable generation, [kWh/m^2]
ψ	characteristic power, [−]

Subscripts

∞	intrinsic property
0	reference
amb	ambient
C	conversion
c	inside the cavern
d	design
e	electricity
G	geostatic
g	natural gas
in	injected
max	maximum
min	minimum
out	extracted
R	rock
r	inside the rock
S	storage
w	at the wall (cavern/rock interface)

Superscripts

max	maximum
min	minimum

Acronym

MILP	Mixed-Integer Linear Program
PtH$_2$	Power to Hydrogen
ROM	Reduced Order Model
SD	Storage Domains
UHS	Underground Hydrogen Storage

but low round-trip efficiencies [9]. This implies that a different fraction of the excess energy, which evolves in time and is proportional to the round-trip efficiency, can actually be stored and re-used through different technologies (Fig. 1-b). Therefore, based on the time scale of the mismatch between energy generation and demand, different solutions are optimal to minimize the energy losses and thus to minimize the carbon emissions.

Underground hydrogen storage (UHS) was already proposed in the 1970s by Gregory et al. [11], Kippenhan and Corlett [12], and Walters [13]. Later, Carden and Paterson [14], and Lindblom [15] have extended the work to a more quantitative analysis with focus on various reservoirs and mined caverns, respectively. Today, among the

large-scale installations that can be used as seasonal energy storage, PtH$_2$ in salt caverns is regarded as one of the most realistic and promising solutions, as salt caverns provide the required capacity and conditions to store hydrogen on a seasonal scale. In particular, the rock is almost impermeable to high pressure gases and the saline environment prevents the onset of biochemical reactions which could consume the hydrogen stored. Furthermore, salt caverns can be operated with relatively high injection and withdrawal rates, and are typically characterized by limited construction costs, especially if the cavern already exists [16]. In the last decades salt formations have been exploited worldwide to store natural gas, oil and chemicals, with hydrogen being successfully stored in two caverns in Texas (US) since 1983, and in three caverns in
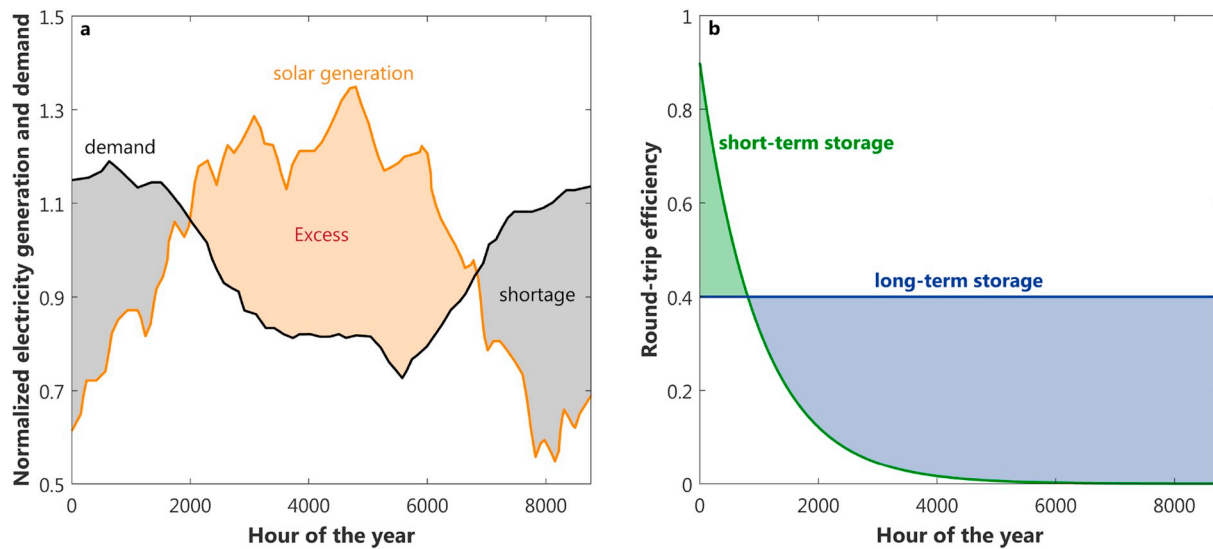
Fig. 1. a) Annual time series of weekly averages that illustrate the seasonal correlation of electricity demand (black line) and solar generation (orange line) for Europe. Electricity generation and demand normalized over the corresponding average value. Figure adapted from Ref. [10]. b) Schematic round-trip efficiency for a short-term (e.g. battery, green line) and long-term (e.g. PtH$_2$, blue line) storage technology. (For interpretation of the references to color in this figure legend, the reader is referred to the Web version of this article.)

Teesside (UK) since 1972 [17]. More recently, different studies investigated the feasibility and the potential of hydrogen storage in salt caverns at different levels, ranging from the analysis of the thermo-mechanical properties of the cavern [18], to the identification of optimal regional sites [19–24], and to the assessment of the financial and environmental performance of underground storage of hydrogen and natural gas [25]. Table 1 provides an overview of recent works on underground H$_2$ storage.

Building on such studies, we aim at bridging technology modeling and system optimization by providing a framework to model underground hydrogen storage that is suitable for the optimization of integrated multi-energy systems (MES). Such systems might be represented by a specific configuration with one spatial node, as considered in this work, or might extend to power-system studies, where the spatial discretization allows for (inter)national studies that include all relevant conversion/storage technologies as well as the electricity grid. To

Table 1
Review of scientific literature focused on underground hydrogen storage (UHS).

Reference	Type of Reservoir	Geographical focus	Approach and topic	Summary of results
Tarkowski [26]	Various	[–]	Theoretical: Roadmap for UHS implementation	Report potential solutions to UHS and delineate the framework of its implementation on an industrial scale.
Tarkowski [19]	Various	Poland	Theoretical: identification of UHS options in Poland	Geological structures in Poland are suitable for any type of hydrogen underground storage.
Stone et al. [20]	Various	UK	Theoretical: identification of UHS options in UK	UK has potential locations where UHS would provide a strategic reserve.
Reitenbach et al. [27]	Various	Germany	Theoretical: effects of H$_2$ on existing natural gas storage facilities	The concentration of hydrogen in the stored natural gas that can be tolerated is limited to some 5–10 vol %.
Bai et al. [28]	Various	China	Theoretical: feasibility and limitations of UHS	UHS criteria: hypertonic porous formations, higher formation pressures, impermeable cap rock, appropriate H$_2$ injection and extraction speed.
Sainz-Garcia et al. [29]	Saline aquifer	Spain	Theoretical: multiphase numerical model of reservoir	Estimated a maximum hydrogen recovery ratio of 78% and a global energy efficiency of 30%.
Pfeiffer et al. [30]	Porous formation	Germany	Theoretical: numerical simulation of storage operation and monitoring	Porous media UHS is a viable option; geochemical reactions and diffusion processes could limit applicability.
Heinemann et al. [31]	Porous formation	UK	Theoretical: practical approach to assess potential UHS in porous media	Carboniferous age sedimentary deposits close to Edinburgh are suitable UHS sites.
Hagemann et al. [32]	Porous formation	[–]	Theoretical: mathematical modeling of UHS in reservoirs	Hydrodynamic behavior of H$_2$ in reservoir is very different from that of natural gas.
Peng et al. [25]	Existing reservoirs	[–]	Theoretical: financial and environmental performance	The most desirable pathway for energy recovery and revenue occurs when H$_2$ is injected along with natural gas and is distributed to off-site users.
Ozarslan [21]	Salt caverns	Turkey	Theoretical: Cavern design issues and safety analyses	Very favourable conditions for a future large-scale integrated plant of hydrogen production, storage and electricity generation.
Michalski et al. [23]	Salt caverns	Germany	Theoretical: investigation of suitable caverns and economic analysis	UHS applicable to north Germany, with capacity of 27 TWh; positive impact on power-systems from optimal implementation of UHS.
Khaledi et al. [33]	Salt caverns	[–]	Theoretical: mechanical response of rock salt	Allowable operating conditions identified: set internal pressure during the cyclic operation so that stresses remain below the dilatancy boundary.
Böttcher et al. [18]	Salt caverns	[–]	Theoretical: numerical model of thermo-mechanical behavior	Large ΔT of H$_2$ may lead to tensile stresses at the cavern boundary; Narrow cylindrical caverns are subjected to a higher risk of structural failure.
Iordache et al. [34]	Salt caverns	Romania	Theoretical: potential use of salt caverns for UHS in Romania	The main components of UHS must be: security of supply, flexibility, production and transmission optimization, infrastructure sizing, market arbitrage.

properly model underground H_2 storage in MES, a new, first-principle thermodynamic model is developed to describe the dynamic behavior of the system when injecting and withdrawing hydrogen. The model accounts for transport phenomena within the salt rock adjacent to the cavern, and allows to fully capture the nonlinear dynamics of the stored energy. As such model is intractable for use in the optimization of integrated systems, a linear reduced order model (ROM) is derived to approximate the performance of the storage for a variety of operating conditions. Such a linear model is then included within a mixed-integer linear program (MILP) optimization framework that allows understanding the role of salt caverns, and the associated PtH_2 technologies when the CO_2 emissions are to be minimized while satisfying the defined energy demand. Accordingly, the key contributions of this work are: (i) a mathematical, first-principle model for the description of underground H_2 storage in salt caverns and reservoirs, (ii) a linear version of the full model that can be efficiently implemented in linear programming and large system optimization while fully retaining the physical behavior, (iii) an improved understanding of the dynamic behavior of underground H_2 storage based on the design and operation of the associated multi-energy system, i.e. renewable generation, electrolyser, fuel cell, and energy storage, and (iv) an assessment of the impact of different time profiles of renewable generation and energy demands on the PtH_2 design and on the CO_2 emissions of the system. It is finally worth stressing, that the system considered here does not have a spatial domain, and does not include the electricity grid and all technologies required for a national power system, e.g. hydropower, carbon capture and storage (CCS), nuclear, as the focus is exclusively on underground H_2 storage and its capability of matching undispatchable renewable generation (which is the only power generation considered here). For power-system studies that investigate the features and feasibility of 100% or close to 100% renewable systems, the reader should refer to the vast relevant literature, e.g. Refs. [5,35–40].

This paper is structured as follows. The thermodynamic model of the salt cavern is described in Section 2 describes the thermodynamic model of the salt cavern. The linear approximation is discussed in Section 3. The optimization framework is presented in Section 4 and the results are discussed in Section 5. Finally, in Section 6 conclusions are drawn.

2. Modeling underground H_2 storage

In this work, we develop a first-principle model for hydrogen storage in underground salt caverns. The model simulates the interaction between the cavern - or, in general, an empty volume - and the surrounding rock when injecting/withdrawing H_2. Because of the general nature of the model equations, the model can be easily specialized to describe

different domains, e.g. underground salt caverns (main focus of the study and represented on the left-hand side of Fig. 2) or depleted gas reservoirs (right-hand side of Fig. 2). The purpose of the model is to describe the dynamic behavior of the stored hydrogen, hence of the stored energy. Especially, we aim at reproducing with reasonable accuracy the behavior of the cavern when cyclically operated as a charging-discharging hydrogen reservoir. In view of site specificity, the preparation phase of the cavern is not described, and the cavern is assumed to be under equilibrium condition when operation is started.

Salt caverns have been operated for decades for salt production. The extremely low permeability and high sealing capacity of salt rock under (near) hydrostatic, upper crustal conditions, is well understood, as are the effects of plastic deformation of the type expected in cavern walls (e. g. Peach and Spiers [41]). More recently, salt caverns have been studied and operated as gas storage reservoirs, especially for natural gas. The behavior of the surrounding salt rock when storing natural gas in the cavern is also rather well understood, and different studies provide detailed analyses of such systems [42–44]. These show that salt rock remains impermeable to gas in the undisturbed region, i.e. where the excavation process has not modified the rock properties. On the contrary, the salt rock develops a limited permeability to gas in the damaged zone (DZ), which is typically confined to a rock depth of less than one radius of the cavern [41,42]. Macro- and micro-fracturing processes occurring during the cavern formation are responsible for the DZ formation. The model presented in this paper builds upon the existing knowledge of salt rock behavior in the case of natural gas storage. While hydrogen properties might result in slightly different quantitative behavior of the rock compared to methane, we argue that the physics underpinning hydrogen storage, and its migration and transport through the rock remain unchanged with respect to natural gas. Accordingly, the spatial domain of the model consists of two connected sub-domains, namely the cavern and the surrounding damaged salt rock. Many mathematical models for underground gas storage found in the literature do not consider the gas flux within (in and out of) the wall ([45–48]). While this approximation has little practical impact for systems such as compressed air energy storage (CAES) - though it might be important to describe cavern integrity - it might affect significantly the performance and the dynamics of H_2 storage. Therefore, the balance equations of our model consider the interaction between the gas in the cavern and that in the salt rock.

The model is based on the following assumptions:

- The cavern has a cylindrical shape, as illustrated in Fig. 2, which is the most appropriate simple description of typical salt caverns worldwide [49].
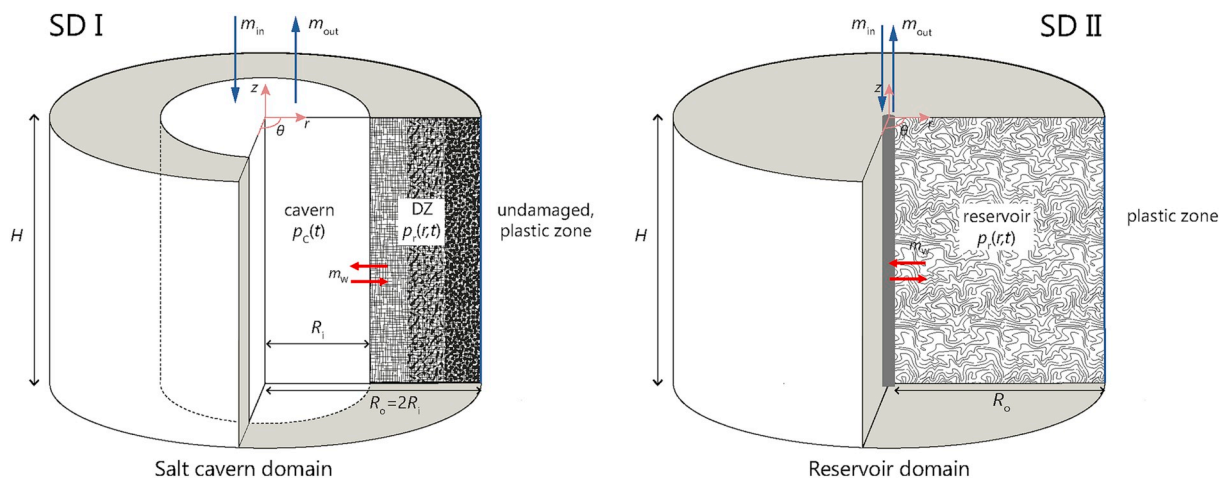

Fig. 2. Schematic of the salt cavern storage described by the first-principle model. Different storage domains (SD) are illustrated, namely salt caverns on the left-hand side (SD I) and gas reservoirs on the right-hand side (SD II).

- The cavern is modeled as a homogeneous spatial domain, i.e. equivalent to a well-stirred tank in other contexts; therefore the hydrogen pressure inside the cavern is function of time only.
- The overall domain is considered isothermal at 40 °C, which has proven to be a good approximation by Raju and Khaitan [45]; this corresponds to the underground temperature at a depth of about 1 km, assuming an average annual temperature of about 10 °C and a geothermal gradient of 31 °C/km [50]. No significant chemical reaction takes place within the domain, i.e. heat is neither generated nor consumed within the cavern and the rock.
- Gas flow through the salt rock is assumed to be one-dimensional along the radial direction (Fig. 2).
- Gas flow through the salt rock is assumed to be single-phase and single-component; although the salt within the excavation zone initially contains 0.1 to 1 vol % brine (saturated salt solution) in intergranular pores and films [51], the model can be reasonably simplified by assuming that after a few storage cycles all the brine is evaporated and the pores are filled with hydrogen.
- The thermodynamic and transport properties of hydrogen are constant, calculated at an average value of the cavern pressure; hydrogen is assumed to be dry, i.e. there is no moisture in the cavern.
- Gravitational effects are neglected due to the low density of hydrogen.

Based on such assumptions, and letting r and t be the spatial and temporal coordinates, the mathematical model consists of the following balance equations:

- Mass balance in the cavern, which describes the dynamics of the hydrogen stored within the cavern:

$$V \frac{d\rho_c}{dt} - m_{in} + m_{out} + m_w = 0 \tag{1}$$

where ρ indicates the hydrogen density and V the cavern volume, $V = \pi R_i^2 H$, with H being the cavern height and R_i the cavern radius; m indicates the mass flow rate; the subscript "c" refers to the conditions inside the cavern, while the subscripts "in", "out" and "w" refer to the mass injected, withdrawn and exchanged through the wall, respectively. All variables, but V, are time dependent. The hydrogen flow through the cavern wall, m_w, is calculated as

$$m_w = \rho_r v A, \quad r = R_i \tag{2}$$

where A is the area of the cavern wall, $A = 2\pi R_i H$, and v is the Darcy

velocity (Eq. (4)); the subscript "r" refers to the damaged region of the salt rock.

- Mass balance of the salt rock, described as a porous medium:

$$\varphi \frac{\partial \rho_r}{\partial t} + \frac{1}{r} \frac{\partial (r \rho_r v)}{\partial r} = 0, \quad R_i \le r \le R_o \tag{3}$$

where φ is the porosity of the damaged zone. The first term on the left-hand side of Eq. (3) represents the rate of hydrogen accumulation within the salt rock, while the second term represents the hydrogen advection.

- Momentum balance of the salt rock:

$$v = -\frac{k}{\mu} \frac{\partial p_r}{\partial r}, \quad R_i \le r \le R_o \tag{4}$$

where k is the hydrogen permeability (Eq. (7)), μ the hydrogen viscosity and p the hydrogen pressure.

The balance equations are solved by using the following constitutive equations:

- Equation of state for the gas phase, both in the cavern and in the rock:

$$p = \frac{\rho R T z}{M} \tag{5}$$

where R is the ideal gas constant, T the system temperature, z the hydrogen compressibility factor averaged at the conditions of interest, and M its molar mass.

- Porosity equation, which expresses a decreasing exponential profile going from the cavern wall to the end of the damaged zone [52]:

$$\varphi = c_1 \exp(-c_2 r), \quad R_i \le r \le R_o \tag{6}$$

where c_1 and c_2 are positive constants, given in the literature for different rock characteristics [41,52,53].

- Permeability equation, with the apparent permeability being calculated as suggested by Klinkenberg [54]:

$$k = k_\infty \left(1 + \frac{b}{p_r}\right) \tag{7}$$

where k_∞ is the intrinsic hydrogen permeability and b is the gas slippage factor. Here, the intrinsic permeability is correlated to the rock porosity

Table 2
Constant parameters used in the mathematical model.

Hydrogen properties ($T = 40\,^\circ$C, $p = 7$ MPa)				
compressibility factor, z	[−]	1.04		
viscosity, μ	[Pa s]	$9.37 \cdot 10^{-6}$		
Storage model		**SD I**	**SD II**	**SD III**
Rock properties				
porosity constant, c_1	[−]	1.38 [52]	6.9 [53]	0
porosity constant, c_2	[1/m]	0.15 [41]	0	0
permeability constant, c_3	[m²]	$1.53 \cdot 10^{-13}$ [41]	10^{-14} [53]	0
gas correction constant, c_4	[Pa/m²]	6.9 [56]	0	0
gas correction constant, c_5	[−]	−0.36 [56]	0	0
Domain geometry and H$_2$ injection/extraction				
inner radius, R_i	[−]	25	0.5	25
outer radius, R_o	[−]	50	1000	–
height, H	[m]		25–300	
cavern depth, D	[m]		100 - 1000	
injected/extracted mass flow rate, $m_{in/out}$	[kg/s]		0.01–10	

by

$$k_\infty = c_3 \varphi^n \tag{8}$$

where $n = 3$, resembling the classical Carman-Kozeny correlation [55], and c_3 is a positive constant based on references [41,52,53]. The gas slippage factor is calculated by using the correlation determined by Jones [56,57]:

$$b = c_4 k_\infty^{-c_5} \tag{9}$$

where c_4 and c_5 are positive constants and b has the same units as p_r.

The values of all the constant parameters appearing in the equations are reported in Table 2.

Combining the aforementioned equations, the following system of partial differential equations is obtained:

$$\widehat{\rho} V \frac{dp_c}{dt} = m_{in} - m_{out} + \frac{\widehat{\rho} kA}{\mu} p_r \frac{\partial p_r}{\partial r}, \quad r = R_i$$
$$\varphi \mu \frac{\partial p_r}{\partial t} = \frac{1}{r} \frac{\partial}{\partial r}\left(r k p_r \frac{\partial p_r}{\partial r}\right), \quad R_i \leq r \leq R_o \tag{10}$$

where the constant $\widehat{\rho} = M/(RTz)$ represents the hydrogen density at unit pressure.

The system of equations given by Eq. (10) is solved with the following set of initial conditions at $t = 0$:

$$p_c = p_{c,0}$$
$$p_r = p_{r,0}(r), \quad R_i \leq r \leq R_o \tag{11}$$

where $p_{c,0}$ is the initial pressure inside the cavern and $p_{r,0}(r)$ is the initial profile of hydrogen pressure inside the salt rock. In this work, initial equilibrium is assumed between the cavern and the rock, hence $p_{r,0} = p_{c,0} = p_0$. The value of p_0 is chosen so as to reflect an average pressure at a suitable depth below the ground.

Furthermore, the following set of boundary conditions is assigned for $t \geq 0$:

$$p_r = p_c, \quad r = R_i$$
$$\frac{\partial p_r}{\partial r} = 0, \quad r = R_o \tag{12}$$

where the former boundary condition is of the Dirichlet type and imposes the continuity of the pressure at the interface between rock and cavern, while the second boundary conditions is of the Neumann type and imposes a zero hydrogen flux through the impermeable rock at the end of the spatial domain corresponding to the damaged zone.

Effectively, different types of hydrogen storage domains (SD) can be simulated depending on the values of the constant parameters c_1-c_5 (Table 2). More precisely:

- SD I, with profiles and values of porosity and permeability resembling the behavior of a H_2 salt cavern (left-hand side of Fig. 2). In this case, the impermeable rock is considered to start at a distance equal to the radius of the cavern, i.e. the inner radius of the rock, R_i. This means that the outer radius, R_o, of the DZ is twice the inner radius and the thickness of the DZ is equal to the radius of the cavern.
- SD II, with constant values of porosity and permeability and a domain geometry that describes the typical behavior of reservoirs (right-hand side of Fig. 2). More specifically, the inner radius is reduced to simulate the H_2 injection/extraction through a pipe, and the outer radius is increased to consider the diffusion through a large rock reservoir.
- SD III, which neglects the rock domain and treats the cavern as a tank with impermeable wall.

In order to simplify the numerical resolution while also laying the ground for the linear model, the following dimensionless variables are

introduced in the system of equations given by Eq. (10):

$$\varepsilon = \frac{\varphi}{\varphi^*}, \quad \kappa = \frac{k}{k^*}$$
$$\Pi = \frac{p_c}{p_{max}}, \quad \pi = \frac{p_r}{p_{max}} \tag{13}$$
$$x = \frac{r}{R_i}, \quad \tau = \frac{t}{t^*}, \quad t^* = \frac{\mu \varphi^* R_i^2}{k^* p_{max}}$$

representing the dimensionless porosity ($0 \leq \varepsilon \leq 1$), the dimensionless permeability ($\kappa \geq 0$), the dimensionless pressure inside the cavern ($0 \leq \Pi \leq 1$) and inside the salt rock ($0 \leq \pi \leq 1$), the dimensionless spatial coordinate ($1 \leq x \leq R_o/R_i$), and the dimensionless temporal coordinate ($\tau \geq 0$), respectively; $\varphi^* = c_1 \exp(-c_2 R_i)$ indicates the porosity at the cavern wall (Eq. (6) for $r = R_i$), $k^* = c_3(\varphi^*)^n$ the intrinsic permeability at the cavern wall (Eq. (8) for $r = R_i$), p_{max} the maximum pressure inside the cavern and the salt rock, and t^* the characteristic cavern time, which can be seen as the ratio of the cavern volume to the volumetric flow rate that can flow through the salt rock. Moreover, the following quantities are introduced:

$$\Gamma = \frac{V p_{max}}{t^*}, \quad \psi_{in/out} = \frac{m_{in/out}}{\widehat{\rho}} \tag{14}$$

indicating the characteristic power capacity of the cavern, Γ, and the injected/extracted hydrogen power, $\psi_{in/out}$. Whereas Γ is a quantity depending on the features of the investigated cavern only, ψ depends on the cavern operation through the injected and extracted flow rates. The resulting system of dimensionless equations that replaces Eq. (10) is:

$$\frac{d\Pi}{d\tau} = \frac{\psi_{in} - \psi_{out}}{\Gamma} + 2\varphi^* \kappa \pi \frac{\partial \pi}{\partial x}, \quad x = 1$$
$$\varepsilon \frac{\partial \pi}{\partial \tau} = \frac{1}{x} \frac{\partial}{\partial x}\left(x \kappa \pi \frac{\partial \pi}{\partial x}\right), \quad 1 \leq x \leq R_o/R_i \tag{15}$$

which is completed by the following initial conditions at $t = 0$:

$$\Pi = \Pi_0$$
$$\pi = \pi_0(x), \quad 1 \leq x \leq R_o/R_i \tag{16}$$

and by the following boundary conditions for $t \geq 0$:

$$\pi = \Pi, \quad x = 1$$
$$\frac{\partial \pi}{\partial x} = 0, \quad x = R_o/R_i \tag{17}$$

The set of Eqs. (15)–(17) is solved by discretizing the spatial domain through finite volumes [58] and by using the stiff solver ode15s implemented in Matlab® for integrating in time.

The developed model is used to investigate the behavior of the stored hydrogen during the typical phases of a storage cycle: (i) an injection phase, where hydrogen is injected in the cavern; (ii) a rest phase at high cavern pressure, where neither injection nor withdrawal occur; (iii) a withdrawal phase, where hydrogen is extracted from the cavern; (iv) a rest phase at low cavern pressure. The optimal storage cycle depends on both storage operation and cavern design. The former includes time profiles of injected and extracted hydrogen mass flow rates, and duration of the rest periods; the latter includes minimum and maximum cavern pressures, cavern depth and volume. Different values of these quantities, which are summarized in Table 2, are considered based on those found in existing installations [59]. Concerning the cavern depth, D, while it does not appear in the mathematical formulation described above, it affects the geostatic rock pressure, which determines the minimum and maximum possible values of hydrogen pressure inside the cavern. Here, such minimum and maximum values are defined as 30% and 80% of the geostatic rock pressure, respectively [60] (see Section 4).

For an illustrative case where the injection, withdrawal and rest phases last 45 days and a constant mass flow rate of 0.2 kg/s is simulated
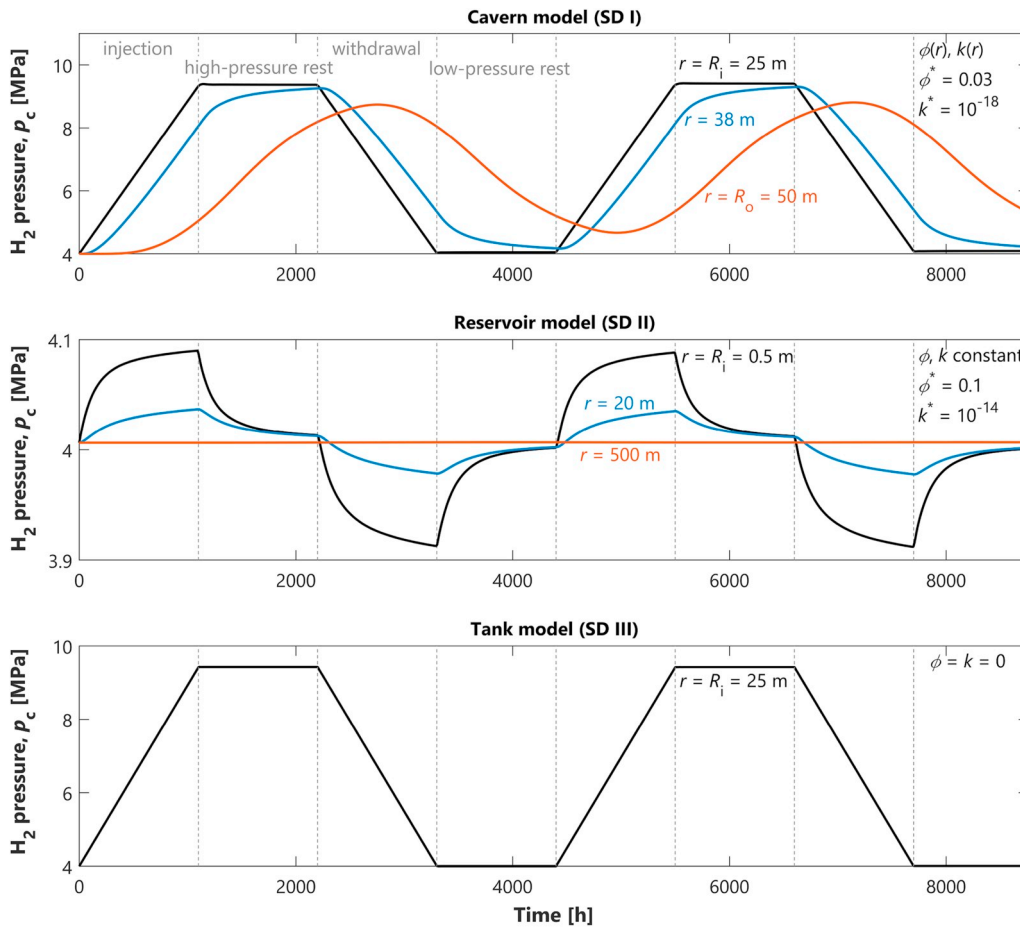
Fig. 3. Time evolution of hydrogen pressure for the three considered domains SD I, SD II and SD III. Hydrogen pressure inside the cavern, p_c, as function of time. Initial conditions: $p_{c,0} = p_{r,0} = 40$ bar. Simulation conditions: injection, withdrawal, and rest phases of 45 days, $m_{in} = m_{out} = 0.2$ kg/s, $H = 100$ m. Hydrogen pressure inside the rock shown for SD I and SD II only.

during both injection and withdrawal phases, the time evolution of hydrogen pressure is reported in Fig. 3 for the three different storage domains SD I to SD III. A cavern height of 100 m is considered; at the beginning of the simulations, the cavern and the rock are at equilibrium at 4 MPa.

During the injection phase the cavern goes from the minimum to the maximum pressure, whereas the opposite happens during the withdrawal phase. Due to the hydrogen diffusion inside the rock domain, the injection and withdrawal phases are followed by cavern-to-rock and rock-to-cavern flows, respectively, during rest periods. More specifically, after the withdrawal phase the hydrogen pressure inside the salt rock is higher than that inside the cavern (rest period at low pressure), and thus hydrogen flows from the rock to the cavern. On the contrary, after the injection phase the hydrogen pressure inside the salt rock is lower than that inside the cavern (rest period at high pressure), thus hydrogen flows from the cavern to the rock.

The resulting pressure profiles during the different phases depend on the type of storage domain, and to the associated set of parameters c_1-c_5. The salt cavern (SD I) features linear profiles inside the cavern and limited change of pressure during the rest phases, i.e. similar to a sealed tank. Similar values of pressure variations are found within the entire rock domain. Conversely, the reservoir (SD II) is strongly affected by the significant permeation of H_2 through the rock domain, resulting in nonlinear profiles close to the injection during all phases of the cycle. On the other hand, because of the relatively large porosity and permeability, the pressure change in time within the reservoir domain is limited, with the maximum variation being smaller than 1 bar, and with no effects at the end of the domain. It is worth stressing that SD II does

not aim at fully representing the complex H_2 injection into a reservoir, but it serves the scope of an exemplary case where H_2 transport is controlled by the rock domain. This will be used to evaluate the capabilities of the linear model derived below, which aims at describing underground hydrogen storage in general, irrespective of any specific features.

3. Linear reduced order models

The detailed model developed in Section 2 is nonlinear, due to the nonlinearity of the model of hydrogen diffusion inside the rock. In the following, the mathematical model is approximated by a system of linear equations, suitable for use within a linear optimization framework. More specifically, (i) constant values are used for the rock porosity, φ, the intrinsic hydrogen permeability, k_∞, and the slippage factor, b; (ii) a change of variables, similar to that proposed elsewhere [61], is performed; (iii) the spatial derivatives are expressed through a polynomial collocation method.

First, a constant value of the rock porosity, $\tilde{\varepsilon}$, is assumed, which implies a constant value of the intrinsic hydrogen permeability, $\tilde{\kappa}_\infty$ (Eq. (8)), hence a constant value of the slippage factor, $\tilde{b}$ (Eq. (9)). This introduces an approximation due to the fact that ε is not constant in reality.

A change of variable is performed by exploiting the expression of the hydrogen permeability (Eq. (7)). More specifically, the quantity $\pi_b = \pi + \tilde{b}/p_{max}$ is introduced, so that $d\pi_b = d\pi$. Then, the system of equations given by Eq. (15) is rewritten by substituting $\zeta = \pi_b^2$ to π:

$$\frac{d\Pi}{d\tau} = \frac{\psi_{\text{in}} - \psi_{\text{out}}}{\Gamma} + \varphi^* \tilde{\kappa}_\infty \frac{\partial \zeta}{\partial x}, \quad x = 1$$

$$\frac{1}{\tilde{\alpha}} \frac{\partial \zeta}{\partial \tau} = \frac{1}{x} \frac{\partial}{\partial x}\left(x \frac{\partial \zeta}{\partial x}\right), \quad 1 \leq x \leq R_o/R_i \tag{18}$$

which is now a linear system in the variables Π and ζ. Here, $\tilde{\alpha} = \frac{\tilde{\kappa}_\infty \tilde{\pi}_b}{\tilde{\varepsilon}}$, $\tilde{\pi}$ is a reference value of the dimensionless pressure inside the rock used to obtain the constant value $\tilde{\pi}_b$, and we use $d\zeta = 2\pi_b d\pi_b$. This introduces an approximation because $\tilde{\pi}_b$ does vary with time and space in reality.

Then, a polynomial collocation method is used to approximate the spatial distribution of the variable ζ. More specifically, ζ is expressed as a second-order polynomial:

$$\zeta(x, \tau) = w_1(\tau) + w_2(\tau)x + w_3(\tau)x^2 \tag{19}$$

where $w_1(\tau)$, $w_2(\tau)$ and $w_3(\tau)$ are time dependent coefficients determining the spatial profile of ζ. In the following, the dependence of w on τ is not indicated for sake of simplicity. Such coefficients are determined by (i) enforcing the boundary conditions, i.e. continuity of hydrogen pressure at the cavern wall (x_1) and zero hydrogen flux at the end of the damaged zone (x_3), (ii) computing the partial differential equation in an intermediate point (x_2).

The boundary conditions are written as

$$x = x_1: \quad \zeta(x_1, \tau) = w_1 + w_2 x_1 + w_3 x_1^2 = \Pi_b^2 = \left(\Pi + \frac{\tilde{b}}{p_{\max}}\right)^2$$

$$x = x_3: \quad \frac{\partial \zeta(x_3, \tau)}{\partial x} = w_2 + 2w_3 x_3 = 0 \tag{20}$$

which result in $w_1 = \Pi_b^2 + w_3 x_1(2x_3 - x_1)$ and $w_2 = -2w_3 x_3$. The differential equation of the salt rock domain is written as

$$x = x_2: \quad \frac{\partial \zeta(x_2, \tau)}{\partial x} = \frac{dw_1}{d\tau} + \frac{dw_2}{d\tau}x_2 + \frac{dw_3}{d\tau}x_2^2 = \tilde{\alpha}\left(\frac{-2x_3}{x_2} + 4\right)w_3 \tag{21}$$

which can be rearranged as

$$2\tilde{\Pi}_b \frac{d\Pi}{d\tau} + \gamma \frac{dw_3}{d\tau} = \alpha w_3 \tag{22}$$

where $\alpha = \tilde{\alpha}\left(\frac{-2x_3}{x_2} + 4\right)$, $\gamma = x_1(2x_3 - x_1) - 2x_2 x_3 + x_2^2$; $\tilde{\Pi}_b$ is calculated by considering a reference value of the pressure inside the cavern, $\tilde{\Pi}$. Finally, the differential equation expressing the hydrogen pressure inside the cavern is given by

$$\frac{d\Pi}{d\tau} = \frac{\psi_{\text{in}} - \psi_{\text{out}}}{\Gamma} + 2\varphi^* w_3 (x_1 - x_3) \tag{23}$$

The set of Eqs. (22) and (23) consists of two ordinary differential equations, which describe the time evolution of the variables Π and w_3 and are linear with respect to both Π and w_3. Therefore, they can be easily implemented within a linear optimization framework. The initial condition for w_3 is determined by assuming a flat profile of the pressure inside the salt rock, and by evaluating the variable ζ in x_2. By considering initial equilibrium between the cavern and the rock, $w_3 = 0$ at $t = 0$.

Different choices of the parameters α, γ and $\tilde{\Pi}_b$, as well as of the collocation points x_1, x_2 and x_3 allow representing the different storage domains introduced in Section 2. More specifically, SD II, which is characterized by constant properties of the rock, is described by $\tilde{\Pi}_b = \tilde{\varepsilon} = \tilde{\kappa}_\infty = 1$; the collocation points are chosen as $x_1 = 1, x_2 = 1.8, x_3 = 3.6$ to describe the steep decrease in rock pressure (Fig. 3); this results in $\alpha = 0.015$ and $\gamma = -3.5$. In contrast, the storage model SD I, where the nonlinear effects due to the hydrogen transport inside the salt rock are
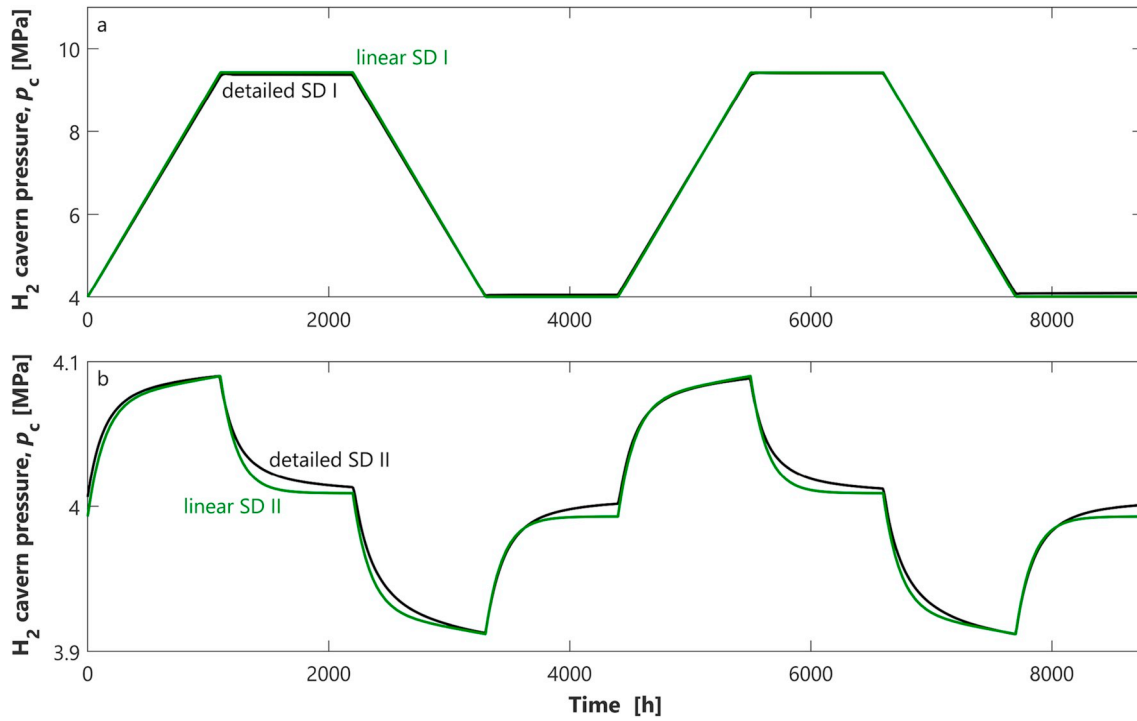
Fig. 4. Comparison between detailed and linear models. (a) Time evolution of hydrogen pressure inside the cavern for detailed and linear SD I. Linear model obtained with $\tilde{\Pi}_b = \tilde{\varepsilon} = \tilde{\kappa}_\infty = \varphi^* = 0$ (no collocation points needed). (b) Time evolution of hydrogen pressure inside the cavern for detailed and linear SD II. Linear model obtained with $\tilde{\Pi}_b = \tilde{\varepsilon} = \tilde{\kappa}_\infty = 1, x_1 = 1, x_2 = 1.8, x_3 = 3.6$. All simulations run with injection, withdrawal, and rest phases of 45 days, $m_{\text{in}} = m_{\text{out}} = 0.2$ kg/s, $H = 100$ m, and uniform initial pressure of $p_0 = 4$ MPa.
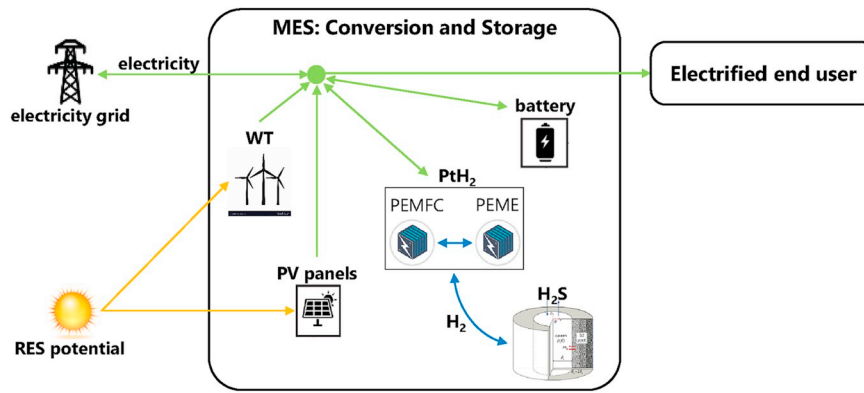
Fig. 5. Schematic representation of the investigated MES including hydrogen storage (HS) in a salt cavern.

negligible, is simply described by choosing $\tilde{\Pi}_b = \tilde{\varepsilon} = \tilde{\kappa}_\infty = \varphi^* = 0$. This corresponds to using the model SD III, and translates in the single ordinary differential equation

$$\frac{\mathrm{d}\Pi}{\mathrm{d}\tau} = \frac{\psi_{\mathrm{in}} - \psi_{\mathrm{out}}}{\Gamma} \qquad (24)$$

Fig. 4 illustrates the comparison between the cavern pressure profiles obtained using the detailed model and those calculated through the linearized model. The linear model of SD I reproduces the detailed model with high accuracy, as the latter is characterized by essentially linear profiles of the cavern pressure across all storage phases (similar to a sealed tank, or SD III). At the same time, the linear model of SD II describes well the corresponding detailed model too: while the more complex pressure profile leads to a slightly larger error between the two models, the key characteristics of the detailed model are well captured by the linear model. Several simulations were run to test the ability of the linear model to match the behavior of the detailed model for a wide range of porosity and permeability values (as an example, the comparison between the linear and detailed model for a permeability two orders of magnitude smaller than that used in the simulations shown in Fig. 4 is reported in Section S3 of the Supporting Information). Overall, the linear model developed proved to be capable of reproducing a variety of underground hydrogen storage domains while allowing for MILP optimization. It is worth noting that this enables the introduction of key optimization constraints, which are required for a realistic operation of underground H_2 storage, as described below.

4. Optimization framework

To reveal the behavior of H_2 storage in salt caverns when optimally operated, and to understand the design of the key components required to produce and convert H_2, the linear model derived in the previous section is plugged into the multi-energy system (MES) framework illustrated in Fig. 5.

Multi-energy systems maximize the potential of high renewable penetration and energy efficiency by exploiting the coupling of different energy carriers (e.g. electricity and hydrogen) both during design and operation [62]. The MES considered in this work is limited to the set of conversion and storage technologies required to produce, store and convert H_2 from renewable power, and it therefore includes: photovoltaic (PV) panels and wind turbines (WT), a power to hydrogen (PtH$_2$) system, which consists of a proton exchange membrane electrolyzer (PEME) converting electricity into hydrogen and a PEM fuel cell (PEMFC) re-converting hydrogen into electricity, and a hydrogen storage (HS) system that couples hydrogen production and consumption. Moreover, lithium-ion batteries are considered at a second stage to study the interaction between long-term H_2 and short-term electricity storage. The goal of the MES is to satisfy the demand of a given end-user, here assumed to be fully electric, while minimizing the CO_2 emissions in a

cost-optimal way. Such CO_2 emissions are related to the carbon intensity of the electricity imported from the grid, which can be used to meet the energy demand when renewable generation is not available at the expense of additional operational costs. In line with the goals of the paper, the MES is simplified to a single node with aggregated energy production, storage and consumption, and is therefore not representative of a full power system, e.g. at national or European scale. The analysis of underground H_2 storage in such power system is beyond the scope of this work.

A mixed integer linear program (MILP) as formulated in Gabrielli et al. [7] is used to determine the minimum-emissions design and operation of the MES. More specifically, we aim at identifying the optimal size and operation of the PtH$_2$ system, i.e. PEME and PEMFC, as well as of the H_2 and battery storage. The overall available storage capacity (H_2 + battery, if present) is treated as a parameter, hence it is not directly determined by the optimizer. The size of the renewable-based technologies is also treated as a parameter, which defines the amount of available renewable energy sources (RES). The MILP can be written in general form as

$$\min_{x,y}\left(f = \boldsymbol{c}^T\boldsymbol{x} + \boldsymbol{d}^T\boldsymbol{y}\right)$$
$$\text{subject to}$$
$$\boldsymbol{A}\boldsymbol{x} + \boldsymbol{B}\boldsymbol{y} = \boldsymbol{b} \qquad (25)$$
$$\boldsymbol{x} \geq 0 \in \mathbb{R}^{N_x}, \boldsymbol{y} \in \{0,1\}^{N_y}$$

where $\boldsymbol{c}$ and $\boldsymbol{d}$ represent the cost vectors associated to continuous and binary variables, $\boldsymbol{x}$ and $\boldsymbol{y}$, respectively; $\boldsymbol{A}$ and $\boldsymbol{B}$ are the constraint matrices for continuous and binary variables, respectively, and $\boldsymbol{b}$ is the constraint known-term; N_x and N_y indicate the dimension of the vectors $\boldsymbol{x}$ and $\boldsymbol{y}$, respectively. The binary variables are introduced to model the operation (on/off scheduling) and costs (size dependency) of the considered technologies. The optimization problem has been described in detail earlier [7], and only the most relevant features are reported in the following, with specific focus on the model of the hydrogen storage, which is described in Section 4.3 (constraints). Additional information, such as costs and performance tables, is provided in the Supporting Information.

4.1. Input data

The input data of the optimization problem are time-dependent profiles with hourly resolution on a year time horizon. Otherwise indicated differently, the bold symbols represent vectors of real numbers with dimension N, where N is the length of the time horizon. Since data are available at every hour of the year, $N = 8760$. The input data are:

1. Ambient conditions: ambient temperature, T_{amb}, solar irradiance, $\boldsymbol{I}$, and wind speed, $\boldsymbol{W}$.
2. Energy demands: the energy demand is here represented by the electricity demand, $\boldsymbol{L}$. This implies assuming a full electrification of
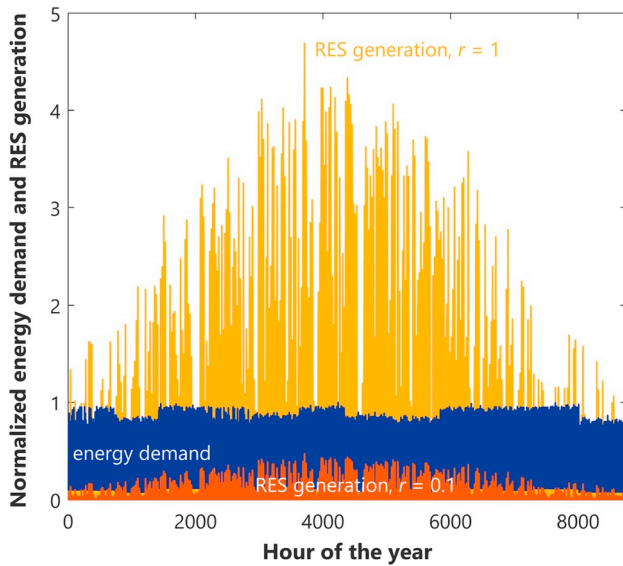
Fig. 6. Illustration of system parameters. Time profiles of energy demand (blue line) and of two different levels of RES generation, namely $r = 0.1$ (red line) and $r = 1$ (yellow line). (For interpretation of the references to color in this figure legend, the reader is referred to the Web version of this article.)

the energy system considered, e.g. thermal demand is satisfied through heat pumps. Such assumption allows for considering the stronger seasonality of heat provision, which is key for long-term storage deployment. The extent to which the heat provision will be electrified is beyond the scope of this work and is discussed in literature, e.g. Refs. [63,64]. Moreover, this assumption allows limiting the portfolio of conversion technologies to those associated with PtH$_2$ and H$_2$ storage, thus enabling a better understanding of the system behavior.

3. Energy prices: import and export electricity prices, $\boldsymbol{u} \in \mathbb{R}^N$ and $\boldsymbol{v} \in \mathbb{R}^{M \times N}$, respectively, where M indicates the number of available technologies. While a constant import price is used, different export prices are considered for RES-based and conventional technologies.

4. Energy environmental footprint: emission rate of electricity grid, ε. Constant and variable time profiles of the CO$_2$ intensity of the electricity grid are considered to account for the time-dependent generation mix of grid electricity in Europe.

5. Technology data: set of available technologies with the corresponding performance and cost parameters; such parameters are reported in Section S1 of the Supporting Information and are taken from Tables 1 and 2 of Ref. [7].

All the values of input data used to perform the calculations presented in the following are discussed in Section S1 of the Supporting Information.

With this work we aim at characterizing the role of H$_2$ storage in salt caverns within a low-carbon energy system, its optimal operation and its interface with PtH$_2$ conversion technologies. We do so by exploring different boundary conditions in terms of potential of renewable energy sources and storage availability, which proved to be the most relevant system parameters when investigating seasonal energy storage within multi-energy systems [7,65]. Indeed, these are simplified metrics whose exact values would be dependent on the power system and the time point in the energy transition. More specifically, we characterize the system based on the following input parameters:

- Available storage capacity, s, defined as the ratio of the maximum stored energy to the annual energy demand. This is a dimensionless parameter calculated as

$$s = \frac{S_{\text{storage}}}{\Lambda} = \frac{\widehat{\rho} V(p_{\max} - p_{\min})h + S_{\text{battery}}}{\Lambda} \tag{26}$$

where $p_{\max}$ and $p_{\min}$ are the maximum and minimum level of cavern pressure, h is the lower heating value of hydrogen, and $\Lambda = \sum_{t=1}^{N} L_t \Delta t$ is the annual energy demand of electricity, with Δt being the duration of the t-th time interval. Here, s varies by varying the cavern volume, V, as well as the battery capacity, S_{battery}, for a given value of Λ and for a fixed maximum pressure inside the cavern. For a given value of s, different time profiles of electricity demand are considered to account for different dynamics induced by different types of energy demand, as described in the following.

- Available RES generation, r, defined as the ratio of annual renewable generation to annual energy demand. This is a dimensionless parameter calculated as

$$r = \frac{E_{\text{renewables}}}{\Lambda} = \frac{\xi a}{\Lambda} \tag{27}$$

where $\xi = \sum_{t=1}^{N} P_t \Delta t$ is the annual renewable generation per unit area and a the area available for the installation of RES-based technologies. In our framework, r varies by varying a (parameter of the optimization problem) for a given value of Λ. For a given value of r, different time profiles of renewable generation are considered to account for the different dynamics characterizing solar and wind generation. Note that curtailment of renewable generation is also accounted for. While this does not lead to a reduction of CO$_2$ emissions, it can lead to a reduction of the system cost by providing flexibility, especially for large shares of renewable energy.

To put r and s into perspective, current values for Europe are in the range of $s = 0.001 - 0.01$ and $r = 0.13 - 0.15$, respectively [66,67]. With the aim of investigating different future scenarios with high penetration of renewable energy sources, we consider wider ranges of such parameters, namely $s = 0.001 - 1$ and $r = 0.1 - 3$ (see Fig. 6). Note that $s = 1$ means that the entire annual energy demand could be stored in the cavern at any given point in time, whereas $r = 3$ implies that RES generate three times the energy requested by the end users, with values > 1 required to cover the efficiency losses of the PtH$_2$ process. Values of s up to 2 were investigated, but did not result in any variation with respect to $s = 1$, and are thus not discussed in the following.

4.2. Decision variables

In the following, the number of available technologies is denoted as M, whereas the number of non-renewable conversion and storage technologies are M_C and M_S, respectively. The following variables are determined by the optimization problem:

Table 3
Constant parameters required to define the cavern constraints within the optimization framework.

Cavern		
Injection/extraction efficiency, $\eta_{\text{in/out}}$	[−]	0.95
Lower fraction of geostatic pressure, δ_*	[−]	0.3
Upper fraction of geostatic pressure, δ^*	[−]	0.8
Maximum hourly pressure variation, $\Delta p_{\max}$	[bar/h]	0.6
Density, ρ_R	[kg/m^3]	2200
Cavern depth, D	[m]	600
Cavern radius, R_i	[m]	25
Compressor		
Low range of pressure ratio, $\beta^{\min}$	[−]	{0; 1; 1.2; 1.6}
High range of pressure ratio, $\beta^{\max}$	[−]	{1; 1.2; 1.6; 2}
Compressor efficiency, $\boldsymbol{\eta}$	[MW/kg]	{0; 0.19; 0.64; 1.13}

1. The size of installed technologies, $S \in \mathbb{R}^M$ ($S = 0$ if a technology is not selected). Whereas the size of renewable-based technologies is fixed by fixing r, the size of the PEM electrolyzer and of the PEM fuel cell, as well as the sizes of H_2 and battery storage, are optimized (with the overall storage capacity being fixed by s). The latter applies if batteries are present in the MES, otherwise the H_2 storage capacity is fixed by s.
2. The scheduling (on/off status) of the non-renewable conversion technologies, $y \in \mathbb{R}^{M_C \times N}$. These include the PtH_2 system (PEME and PEMFC) and the compressor required to inject H_2 at the cavern pressure.
3. The input and output power flows of all available technologies, F and $P \in \mathbb{R}^{M \times N}$, respectively.
4. The energy stored in the storage technologies, $E \in \mathbb{R}^{M_S \times N}$.
5. The imported and exported electricity, $U \in \mathbb{R}^N$, and $V \in \mathbb{R}^{M \times N}$, respectively. The latter varies with the technology due to the different export prices.

4.3. Constraints

The constraints of the optimization problem can be grouped into two categories:

1. Behavior of conversion and storage technologies. The constraints adopted to model the performance of the PtH_2 system are described in detail in Ref. [68], with the methodology TM I being implemented here, i.e. piecewise affine correlations accounting for partial-load performance and minimum-power requirements. The constraints used to model the performance of the PV panels are described in Ref. [7], whereas the constraints used to model the performance of the wind turbines are described in Section S2 of the Supporting Information. The behavior of the salt cavern is described by Eq. (10), where the flux across the cavern wall is neglected (according to the linear model described in Section 3) and by discretizing in time as:

$$p_{c,t+1} = p_{c,t} + \frac{1}{\bar{\rho}V}(m_{in,t} - m_{out,t})\Delta t \tag{28}$$

Here the inlet and outlet mass flow rates account for H_2 losses during injection and withdrawal via the charging and discharging efficiency, η_{in} and η_{out}, respectively:

$$m_{in} = \eta_{in} m_{out}^{PEME}, \quad m_{out} = \frac{m_{in}^{PEMFC}}{\eta_{out}} \tag{29}$$

It is worth noting that the time discretization in hourly intervals is appropriate to describe the slow cavern dynamics. All the parameters required to define the constraints of the optimization problem are summarized in Table 3.

The following periodicity constraint is imposed to assure that the same energy is stored at the beginning and at the end of the time horizon:

$$p_{c,1} = p_{c,N} \tag{30}$$

Furthermore, a number of constraints must be considered to ensure the cavern integrity over time. These constraints are expressed as function of the cavern pressure. The first constraint sets the cavern pressure between a lower and an upper value. These are expressed as fractions of the geostatic pressure, p_G, which depends on the depth of the cavern, D. Thus, for all time instants $t \in \{1, ..., N\}$:

$$\delta_* p_G \leq p_{c,t} \leq \delta^* p_G \tag{31}$$

where δ_* and δ^* are the lower and upper fractions, respectively; the geostatic pressure is defined as $p_G = \rho_R g D$, where ρ_R is the density of the rock and g is the gravity acceleration. Here, the depth of the cavern is

fixed, with $D \gg H$, which allows considering a constant value of the geostatic pressure.

The second constraint limits the rate of variation of the cavern pressure for all time instants as

$$|p_{c,t+1} - p_{c,t}| \leq \Delta p_{max} \tag{32}$$

where Δp_{max} is the maximum hourly pressure variation that can be endured by the cavern.

Finally, the electricity consumption required to compress the hydrogen from the pressure of the synthesis process, p_E, to that of the cavern must be considered. A thermodynamic model of a two-stage compressor is built in Aspen-Plus® [69] and then linearized. In particular, the nonlinear dependency of the electricity consumption on the pressure ratio, $\beta = p_c/p_E$, is described through a piecewise constant approximation, which also allows eliminating the bilinearity between the pressure ratio and the mass flow rate:

$$F = m_{in} \sum_{i=1}^{n} \eta_i y_i \tag{33}$$

with

$$y \cdot \beta^{min} \leq \beta \leq y \cdot \beta^{max}, \quad y \cdot 1 \leq 1 \tag{34}$$

Here, the constant coefficient η_i, for all $i \in \{1, n\}$, is used to approximate the compressor efficiency within the i-th range of pressure ratio $[\beta_i^{min}, \beta_i^{max}]$, which is selected by the binary variable $y_i \in \{0, 1\}$. Due to the concavity of the curve, and since the energy consumption must be minimized, a binary variable for each pressure range is required [70]. The constant coefficient η, as well as the ranges of pressure ratio considered here ($n = 3$), are reported in Table 3. A graphical comparison between the original and the simplified compressor model is reported in Section S4 of the Supporting Information.

2. Energy balances of the integrated energy system. The energy carriers considered in this work are electricity (e) and hydrogen (H_2). More specifically, electricity is used by the PEME to generate hydrogen and it is required by the end-user, whereas hydrogen is re-converted by the PEMFC into electricity and it is stored within the cavern. For all energy carriers $j \in \{e, H_2\}$ the sum of imported and generated power must equal the sum of exported and used power for all time instants $t \in \{1, ..., N\}$. In general, this can be written as

$$\sum_{i=1}^{M} (P_{j,i,t} - F_{j,i,t} - V_{j,i,t}) + U_{j,t} - L_{j,t} = 0 \tag{35}$$

where P is the generated energy, F the consumed energy, V the exported energy, U the imported energy, and L the energy required by the end user. No limitations on the imported and exported energy are considered here.

4.4. Objective function

The optimization problem determines the optimal design and operation of the MES, which satisfies the energy demand while minimizing the CO_2 emissions in a cost-optimal fashion. The annual CO_2 emissions of the system, e, are calculated based on the amount of imported electricity:

$$e = \sum_{t=1}^{N} \varepsilon_t U_t \Delta t \tag{36}$$

where ε is the CO_2 emission rate of the electricity grid (see Section S1 of the Supporting Information). The total annual cost of the system, J, includes the capital, operation and maintenance contributions, which are calculated as thoroughly described in Ref. [7].

Since both CO_2 emissions and operation costs are calculated based on the amount of imported electricity, minimizing the CO_2 emissions
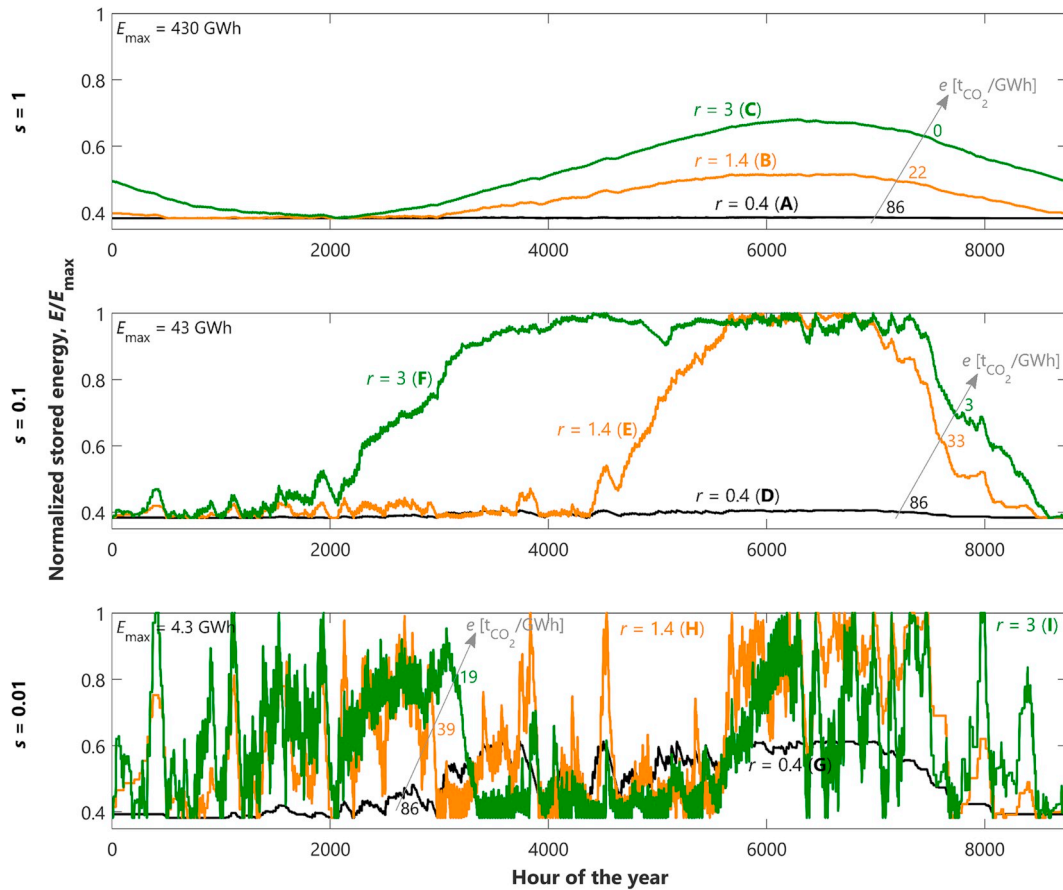
Fig. 7. Impact of r and s on the optimal operation of the H$_2$ storage. Stored energy, E, normalized over its maximum value (available storage capacity), is reported at every hour of the year for $r = 0.1, 1, 3$ and $s = 0.001, 0.1, 1$.

corresponds to minimizing the operation costs, with the capital cost of the system being a consequence of this choice. The capital cost of the cavern is not included in the computation of the total annual cost, as we consider the use of existing caverns, whose cost is assumed to be already amortized at the beginning of the operation. Reference costs for existing salt caverns can be found in the literature [60]. Moreover, adding the cavern costs would not change the findings, but for the levelized cost of energy storage, which is of minor importance in this study.

To obtain the minimum-emissions design in a cost-optimal way (e.g. avoiding useless oversizing of the PtH$_2$ system), both the CO$_2$ emissions and the costs of the system must be included in the objective function of the optimization problem, f. Therefore, f is built as a combination of e and J, with e being prioritized by means of two scaling factors, e_0 and J_0:

$$f = \frac{e}{e_0} + \frac{J}{J_0} \tag{37}$$

The value of J_0/e_0 depends on the order of magnitude of the two objectives [71]; here, a value of $J_0/e_0 = 10^5$ is utilized.

5. Results and discussion

In the following, the linear model SD I is used to investigate the potential of H$_2$ storage for reducing the CO$_2$ emissions of the considered integrated energy system, as salt caverns represent a realistic and promising option for large-scale, long-term energy storage. The optimization framework introduced above is applied to investigate the optimal design and operation of MES as in Fig. 5, for different profiles of energy demand, renewable generation and environmental footprint of the electricity grid. First, no battery capacity is considered ($S_{battery} = 0$) to fully focus on the role of H$_2$ storage. More specifically, the storage

operation, the size of the PtH$_2$ system, and the CO$_2$ emissions of the systems are studied as function of the available RES generation, r, and storage capacity, s.

5.1. Optimal system operation

First, we study the optimal operation of a refernce MES defined by considering (i) a relatively flat electricity demand across the year, i.e. neglecting the seasonal periodicity induced, e.g. by the heat demand, (ii) solar-based RES generation, i.e. not considering the wind turbines within the MES of Fig. 5, and (iii) constant CO$_2$ emission rate of the electricity grid. We analyze the effect of available storage capacity and RES generation on the optimal operation of the H$_2$ storage, as illustrated in Fig. 7, where the evolution of H$_2$ storage along the year is plotted for three different values of r and s (denoted by points A-I on the (r,s) plane in Fig. 9).

The following storage behaviors are observed:

- At large values of the ratio s/r, e.g. $r = 0.4$ and $s = 1$ (point A), a flat storage profile is obtained as energy storage is not needed due to the lack of renewable generation.
- At small values of the ratio s/r, e.g. $r = 3$ and $s = 0.01$ (I), daily and weekly storage cycles prove to be optimal as seasonal storage profiles are prevented by the limiting storage capacity. Indeed, the combination of low storage capacity and high RES generation makes shorter cycles mandatory to compensate for the daily variation of the available renewable energy.
- At intermediate values of the ratio s/r, e.g. $r = 3$ and $s = 1$ (C) or $r = 1.4$ and $s = 0.1$ (E), seasonal storage cycles occur as the large storage
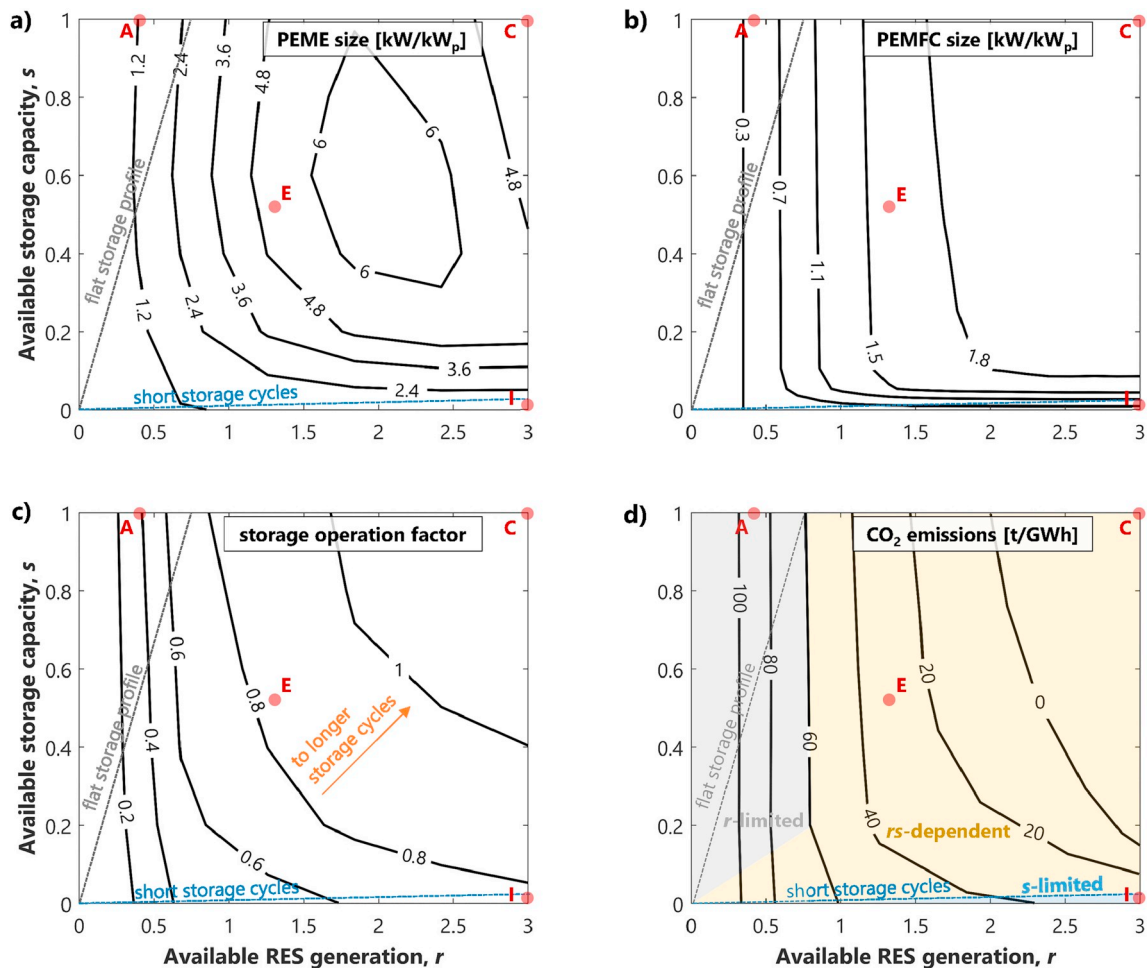
Fig. 8. Impact of r and s on the optimal system design and CO_2 emissions for reference input data. System characterized in terms (a) of size of PEM electrolyzer and (b) size of PEM fuel cell, (c) of storage operation factor, and (d) of specific CO_2 emissions. Three different regions are identified based on the storage operation, characterized by flat (on the left of gray dashed line), daily/weekly (below blue dashed line), and seasonal storage cycles (remaining section of the plane). Three different regions are identified in terms of CO_2 emissions, with r being the limiting factor (gray shaded area), s being the limiting factor (blue shaded area), and both r and s allowing emissions reduction (yellow shaded area). The shape of the regions depends on the resolution of the optimizations performed with respect to r and s. Exemplary points A, C, E, I reported for comparison with Fig. 7. (For interpretation of the references to color in this figure legend, the reader is referred to the Web version of this article.)

capacity and RES generation result in smooth charging and discharging phases.

This confirms that a large storage capacity is required to fully exploit the potential of seasonal storage technologies, which is further amplified for larger amount of available RES. Furthermore, the storage operation is quantified by looking at how the storage is exploited. At low values of r, e.g. $r = 0.4$, the H_2 storage is not well exploited, with a maximum stored energy equal to about 0.5%, 4%, and 37% of the maximum value for $s = 1$ (A), 0.1 (D), and 0.01 (G), respectively. At low values of s, e.g. $s = 0.01$, the H_2 storage is operated with non-seasonal dynamics, with about 45%, 80%, and 85% of all cycles being shorter than a week for $r = 0.4$ (G), 1.4 (H), and 3 (I), respectively.

Fig. 7 also shows that at low values of r the CO_2 emissions are independent of the value of s, with the lack of RES generation being the limiting factor. On the contrary, for larger values of r smaller CO_2 emissions are obtained by increasing s. The CO_2 emissions of the MES, together with the corresponding design, are discussed below with reference to the (r,s) plane (Fig. 9).

5.2. Optimal system design

The storage operation affects the minimum-emissions system design,

which is first investigated for the reference MES defined above.

Based on this, the minimum-emissions design is studied for values of r from 0.1 to 3 and values of s from 0.001 to 1, and is illustrated in Fig. 8, which shows (a) the size of the PEM electrolyzer and (b) of the PEM fuel cell, (c) the storage operation factor, and (d) the value of specific CO_2 emissions. The storage operation factor is defined as the number of hours in which the H_2 cavern is operated, either in charging or in discharging modes, divided by the total number of hours in the year; the specific CO_2 emissions are obtained by normalizing the annual CO_2 emissions over the annual electricity demand.

Concerning the PtH_2 system, the following considerations can be made:

- At large values of the ratio s/r, e.g. $r = 0.4$ and $s = 1$ (point A on the (r,s) plane), the sizes of PEME (Fig. 8-a) and of PEMFC (Fig. 8-b) are independent of s since the shortage of renewable generation limits the operation of the PtH_2 unit.
- At small values of the ratio s/r, e.g. $r = 3$ and $s = 0.001$, the sizes of PEME and of PEMFC are independent of r since the lack of storage capacity limits the operation of the PtH_2 unit.
- At intermediate values of the ratio s/r, e.g. $r = 3$ and $s = 1$ (C) or $r = 1.4$ and $s = 0.1$ (E), the sizes of PEME and of PEMFC are function of both r and s. More specifically, the size of the PEME presents a
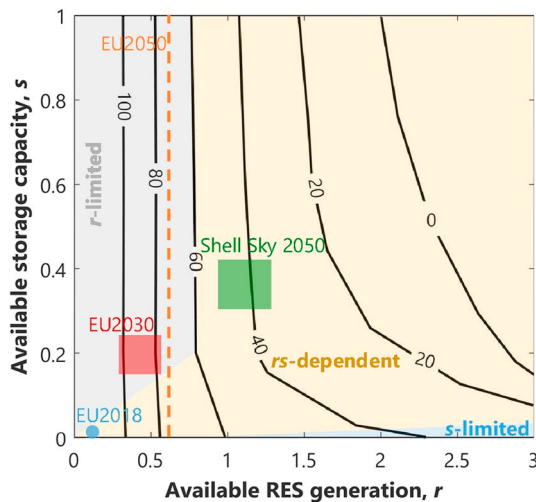
Fig. 9. CO_2 emissions regions on the (r,s) plane and comparison against present and future values of r and s as reported by: EU 2018 (blue circle [66]), high renewable EU 2030 (red area [73]) and EU 2050 (orange dashed line [74]), and Shell Sky (green area [75]). (For interpretation of the references to color in this figure legend, the reader is referred to the Web version of this article.)

maximum with both r and s, with the biggest sizes being installed for $s = 1$ at $r = 2$. On the one hand, at large values of s/r (C) the storage is large with respect to the energy demand and to the amount of renewable generation that must be stored to reduce the CO_2 emissions. In this case, the size of the PEME can be limited by operating the storage with a seasonal pattern, characterized by smooth charging and discharging phases. On the other hand, going towards smaller values of s/r (from point E to I) the storage is small with respect to the energy demand and to the available renewable generation, which results in shorter-term storage dynamics and in smaller PEME sizes. The maximum of the PEME size as function of r occurs because of the trade-off between the available renewable energy that can be stored and that needs to be stored to reduce the CO_2 emissions: The size of the PEME decreases when either the former or the latter is limiting.

- The size of the PEMFC increases when increasing s and r, reaching an asymptote in both cases. The dependency on s depends on the amount of hydrogen available from the storage. The asymptotic PEMFC size is reached either when $e = 0$ t/GWh, i.e. when zero CO_2 emissions are achieved, or when s starts being limiting for the PEMFC operation. Indeed, as $e > 0$ the emissions can be driven down by using more of the RES generation through the PtH_2 system, hence increasing the size of the PEMFC; once $e = 0$, there is no reason for the size of the PEMFC to increase. Likewise, there is no reason for larger PEMFC once the available amount of hydrogen is limited by the storage size (e.g. for the entire r range in case $s = 0.001$).
- The cavern operation factor (Fig. 8-c) increases with both s and r. This means that the cavern is operated for more hours when larger or when, for a given volume, the amount of renewable generation increases.

Concerning the CO_2 emissions (Fig. 8-d), they decrease when increasing r and s. This is fairly intuitive, as a greater emissions reduction is achieved when increasing the amount of RES generation and of storage capacity, i.e. increasing the fraction of RES generation that can be shifted in time. More interestingly, three different regions are identified: (i) an r-limited region, below a given value of r, where the CO_2 emissions cannot be reduced by increasing s, (ii) an s-limited region, below a given value of s, where the CO_2 emissions cannot be reduced by increasing r, (iii) an rs-dependent region, above given values of r and s where the CO_2 emissions can be reduced by increasing either r or s.

5.3. CO_2 emissions regions

While in the previous sections we have focused on the analysis of the optimal MES design and operation, as well as of the interplay between the two, we now discuss more in detail the CO_2 emissions of the system, with the aforementioned regions being reported in Fig. 9. Note that the zero-emissions line quantifies the minimum storage capacity required for the considered MES to achieve zero CO_2 emissions for a given RES availability. The same holds for any value of CO_2 emissions, where the corresponding line identifies the minimum storage capacity required to reach the corresponding level of CO_2 emissions for a given value of RES generation. Here we consider the carbon intensity of the Swiss electricity grid as reference, i.e. 137 t_{CO_2}/GWh [72]. While a different, yet constant, carbon intensity of the grid would shift the curve towards lower or larger s-r when having lower or larger CO_2 intensity, respectively, it would not affect the trends and conclusions that can be drawn from Fig. 9.

Fig. 9 put the calculated CO_2 emissions in perspective with present and future values of r and s. We consider the current European values (EU 2018 - blue circle [66]), the European high renewable scenario for 2030 (EU 2030 - red area [73]) and for 2050 (EU 2050 - orange dashed line [74]), and the 2050 Shell Sky scenario (green area [75]). While for Shell Sky it was possible to calculate the difference between renewable primary energy and renewable-based delivered electricity, thus accounting for storage losses, for EU 2050 the data provided are for gross electricity production, thus accounting for transportation losses but not for storage losses. Moreover, for EU 2050 no data is reported for the required storage capacity, and we thus report the available RES generation only, whereas s can be inferred from Shell Sky data as about $s = 0.38$ for 2050 and $s = 0.54$ for 2100. Concerning the EU 2030 scenario, the ranges of s and r are calculated based on the countries reported in a recent EU study (namely Germany, Denmark, Spain, France, Italy, Greece, Ireland, Poland and Romania), which calculates the effect of high renewable shares on the grid storage requirements [73]. It is worth noting that the considered future scenarios when coupled to a H_2 based system would result in a reduction of CO_2 emissions with respect to the current situation (Fig. 8), but not lower than 60 t_{CO_2}/GWh. Interestingly, based on European emissions predictions, the EU 2050 scenario would result in values of CO_2 around 80 t_{CO_2}/GWh [74], which is in line with our calculations for a simpler system. As mentioned above, more ambitious scenarios for a 100% renewable system are reported in scientific power-system studies, e.g. Refs. [5,35–40]. Such r-s graph, which is here quantified exclusively for a H_2-based system in Fig. 9, can be used to identify needs and gaps in reaching zero-emissions electricity provision based on non dispatchable renewable generation. It is in fact worth remembering that staying below 1.5 °C requires having net zero emission by mid-century.

As expected, each point on the zero-emissions line features different costs: Moving along the line, the cost of the energy system presents a minimum at $r = 2.4$ and $s = 0.5$ (330 EUR/MWh), passing from 370 EUR/MWh at $r = 3$, $s = 0.11$ to 410 EUR/MWh at $r = 2$, $s = 1$. This implies that increasing the storage capacity, in this case given by the PtH_2 system, allows reducing the system cost until a value of $s = 0.5$, while above this threshold the cost increases. This is due to the design of the PtH_2 system, and specifically to the size of the electrolyzer (Fig. 8), which decreases moving from $(r = 2, s = 1)$ to $(r = 2.4, s = 0.5)$ and then increases from $(r = 2.4, s = 0.5)$ to $(r = 3, s = 0.11)$. Overall, the PtH_2 system represents the main cost to achieve zero-emissions energy systems, with the PEM electrolyzer (PEME) representing the major contribution of the system capital cost (average of 70%), followed by PVs (average of 16%) and PEMFC (average of 14%) - unit cost of electrolyzer and fuel cell for the installed size of interest is 1350 EUR/kW and 1320 EUR/kW, respectively [76]. The total system costs are entirely due to the capital contribution. Indeed, the operation costs are connected to amount of energy imported from the grid, hence proportional to the CO_2 emissions. Clearly, these costs do not reflect the optimal values for
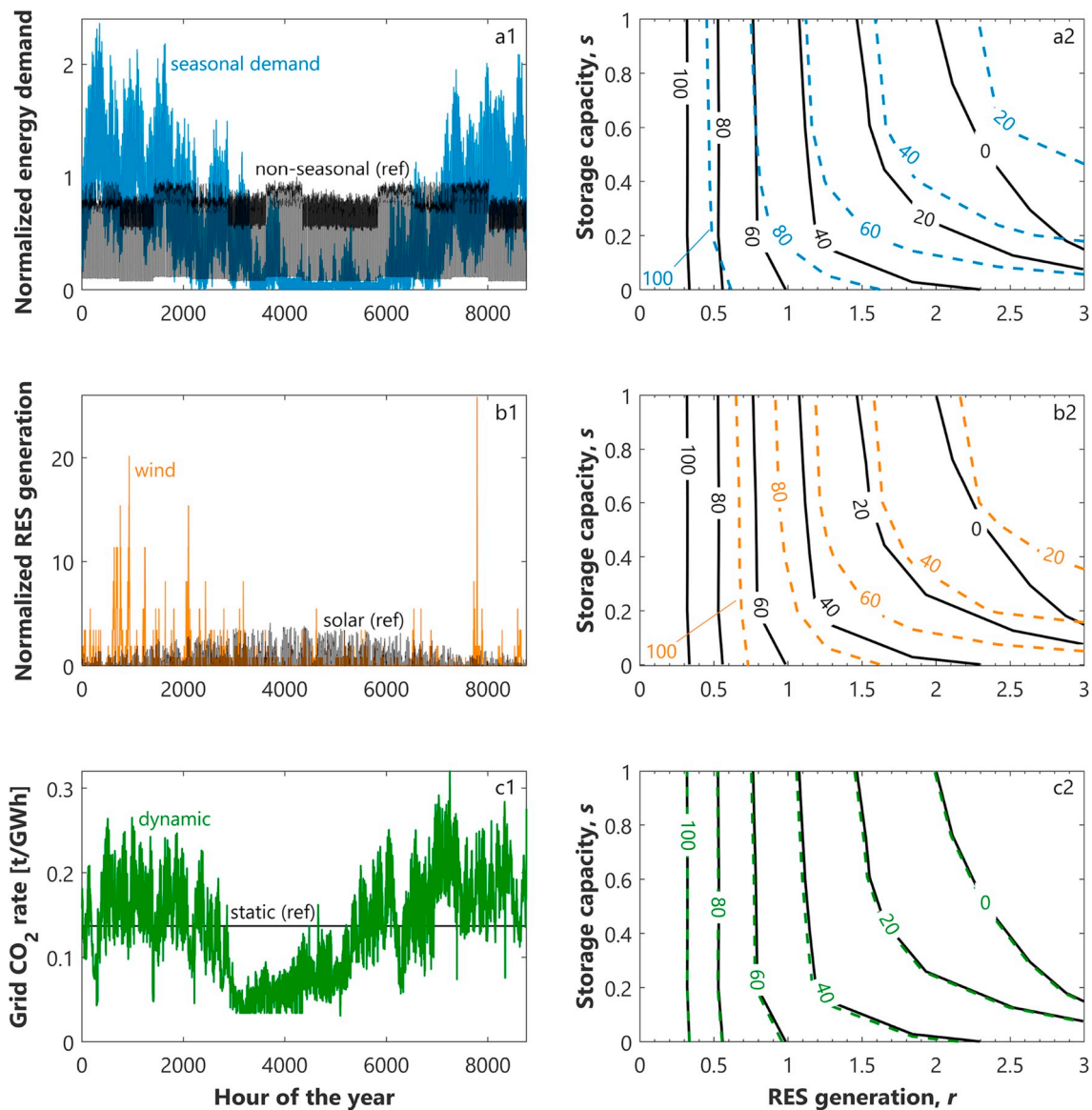
Fig. 10. Impact of input data time profiles on CO_2 emissions regions: (a) seasonal energy demand, (b) wind-based RES generation, and (c) variable carbon intensity of the electricity grid. The time profiles of the considered input data are shown on the left-hand side (sub-Fig. 1). The emission regions on the (r, s) plane are shown on the right-hand side (sub-Fig. 2). Same color code applied for the new emissions maps and the new profiles of input data. (For interpretation of the references to color in this figure legend, the reader is referred to the Web version of this article.)

a100% renewable power-system, which are typically in the range of 50–120 EUR/MWh [37,38,77–79], but exclusively the H_2-based system investigated here. In fact, the higher costs of such system confirm the need of adopting a portfolio of different technologies and measures.

5.3.1. Impact of input data profiles

So far, we have investigated the optimal MES design for a reference set of boundary conditions featuring an electricity demand with daily variability, but no seasonal fluctuations along the year, a solar-based renewable generation profile, and a flat carbon intensity of the electricity grid. However, the time profiles of all such factors strongly impact the system design. Therefore, in this section we evaluate the impact of (i) a seasonal energy demand accounting for the periodicity induced, e.g., by electrified heating, (ii) wind-based renewable generation, (iii) time-dependent carbon intensity of the electricity grid. A sensitivity analysis on the operating pressure of the PEM electrolyzer, which determines the pressure of the generated H_2, was also performed. However, it was found to have little impact on the final values of CO_2 emissions, and

therefore all simulations presented are for a reference pressure of 5 MPa [68,80].

Concerning the PtH$_2$ system, while similar considerations hold for the size of electrolyzer and fuel cell, the variations of the input data mostly affect the former. Indeed, whereas the H_2 generation is directly affected by the time-profiles of the input data, the H_2 production behaves according to the storage availability and the input data. The design of the PtH$_2$ system as function of r and s for the new input data is reported in Section S5 of the Supporting Information, while here we focus on the emissions regions. Fig. 10 reports the resulting maps (right-hand side) for different time profiles of the considered input data (left-hand side). The reference case is always represented as in Figs. 8 and 9 (black solid lines in the right-hand side figures), and the same isolines are reported for the different input data (gray dashed lines in the right-hand side figures).

Seasonal fluctuation in the energy demand. A seasonal dynamics of the energy demand, typically high in winter and low in summer in cold climates, emphasizes the mismatch between the demand and the
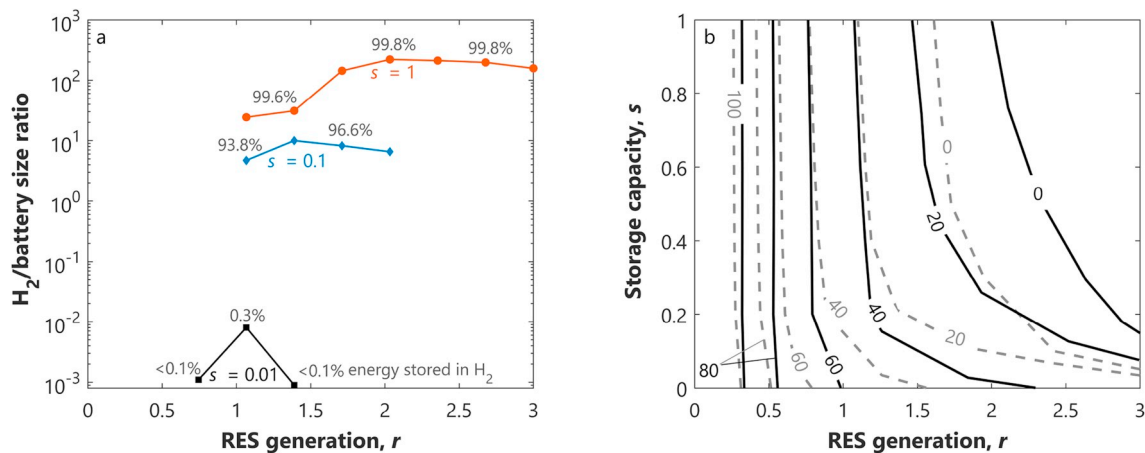
Figure 11. Impact of r and s on the optimal system design and CO_2 emissions for two energy systems featuring H_2 storage only (solid line) and a combination of battery and H_2 storage (dashed line). Results presented in terms of (a) H_2 storage-to-battery size ratio and fraction of annual energy stored in H_2 storage (gray numbers above the lines), (b) CO_2 emissions regions. Three values of s are reported, namely 0.01 (black squares), 0.1 (blue diamonds), and 1 (red circles).

solar-based renewable generation, which is high in summer and low in winter. This makes more difficult the exploitation of renewable generation, hence resulting in higher CO_2 emissions for given RES generation and storage capacity (Fig. 10-a2). In this case, the zero-emissions region is not attainable with the r-s limits considered, and the 60 t/GWh emission line is shifted towards higher values of r. Furthermore, a seasonal dynamics of the energy demand translates into a more seasonal operation of the H_2 storage. This results in smaller PEME at low values of r, where the available RES can be stored by operating the storage through smooth charging and discharging phases, and in bigger PEME at high values of r and s, where the storage capacity is still sufficient to store the available RES, but a sharper charging is required. On the contrary, if the peak demand is in summer, e.g. tropical or south-European countries, the zero-emissions region is achieved for lower r and s values (see Section S5 of the Supporting Information).

Wind-based renewable generation. Similar trends are observed when comparing solar- and wind-based RES generation, in Fig. 10-b. In this case, the reference (non-seasonal) energy demand is considered. The wind-based generation is characterized by a lower seasonality than the solar-based one, while it presents much higher peaks during the winter season. This translates into a significantly larger size of the electrolyzer, which must be able to exploit the sharp generation surplus when storage capacity is available. Similar sizes of the electrolyzer are obtained when decreasing s, as the storage capacity becomes the limiting factor for reducing emissions. Higher CO_2 emissions are obtained with respect to solar generation due to the difficulty in exploiting the spikes of wind generation (Fig. 10-b2). Again, the zero-emissions region is not attainable, and higher values of renewable generation and storage capacity are needed to achieve CO_2 emissions of 60 t/GWh. If solar and wind are combined, the zero-emissions region moves remarkably to the left for $s = 0.2 - 0.8$ (see Section S5 of the Supporting Information). In this case, smaller sizes of the electrolyzer are obtained.

Variable grid carbon intensity. Concerning the emission factor of the electricity grid, reported in Fig. 10-c, the variable profile considered here is characterized by higher values in winter due to the presence of fossil fuels power plants, and lower values in summer due to abundant renewable generation [72]. The same mean value of the constant profile is kept. Such a dynamics of the grid emission factor enhances the role of H_2 cavern and of the PtH$_2$ system. Indeed, during the summer the storage does not only offset the mismatch between high renewable generation and low energy demand, but it also allows to exploit the low-carbon electricity produced in summer during periods of high-carbon electricity during winter. This translates in slightly lower CO_2 emissions, and higher sizes of the electrolyzer, at values of s for which there is available storage capacity to exploit the low-carbon grid

electricity and such a low-carbon electricity is still needed to drive the CO_2 emissions to zero ($s = 0.01 - 0.1$). Similar emissions and sizes are obtained otherwise. Overall, the difference between constant and variable profiles is rather limited. It is worth noting that, as long as the minimum-emissions design is investigated and the shape of the time profile is fixed, the specific value of the carbon intensity affects the amount of emitted CO_2 only, whereas it has no influence on the system design. Furthermore, it does not affect the zero-emission regions, which rely on distributed generation only (no grid contribution) to satisfy the energy demand.

5.3.2. Impact of combining short- and long-term energy storage

Up to now, we have considered the H_2 cavern as a stand-alone energy storage system. While this is characterized by negligible losses, it features a low round-trip efficiency, which makes it not suitable for offsetting short-term mismatch between renewable generation and energy demand. To address this point and to understand the impact of short-term storage systems on underground H_2 storage, we study the coupling of H_2 and battery storage, i.e. we refer to the MES illustrated in Fig. 5 without enforcing the size of the battery equal zero. In this case, the sum of the sizes of battery and H_2 storage ($s_{battery} + s_{H_2}$) is limited by the overall available storage capacity, defined by s. The optimization determines the optimal combination of sizes, i.e. the optimal way to exploit the storage capacity, to minimize the system emissions in a cost-optimal fashion. The emissions regions of the two MES are presented in Fig. 11-b, while the ratio of H_2 storage to battery size and the fraction of energy stored in the H_2 storage (gray numbers above the symbols) are reported in Fig. 11-a.

The combination of H_2 and battery storage leads to a smaller PtH$_2$ system with respect to the case with H_2 storage only (as shown in Fig. S5 of Section S6 of the Supporting Information). In fact, at low values of r ($r \leq 1$) or at low values of s the RES generation is stored entirely in the battery, which provides a higher round-trip efficiency and lower overall energy losses than H_2 storage, and no PtH$_2$ is installed. In contrast, PtH$_2$ is selected at higher values of r, when the amount of RES justifies long-term energy storage. In this case, the H_2 storage is operated in a seasonal fashion (with one storage cycle per year), while battery is operated through daily or weekly cycles (with 200–250 storage cycles per year). In fact, the seasonal behavior of H_2 storage is more pronounced when coupling it with the battery, since this removes the necessity to offset short-term variability. At very low s, e.g. $s = 0.01$, only batteries are installed, as the storage is operated in a short-term fashion. However, at larger s, both the battery and the H_2 storage must be used, with H_2 storage being predominant for $s \geq 0.1$, where it features sizes 10 to 200 times larger than the battery and it stores more than 90% of the total

energy stored annually. This result is indeed valid for the system configuration and boundaries considered in this work; batteries storage is expected to play a larger role in a power-system considering all possible conversion technologies and policies. As expected, combining short- and long-term energy storage allows reducing the CO_2 emissions for given storage capacity and RES generation (Fig. 11-b). In this case, the emissions curves are shifted towards lower values of r and s, with the greatest benefit of the battery being observed at intermediate values of s: at low values of s (e.g. $s = 0.001$) there is not much room for improvement as the CO_2 emissions cannot go to zero even for high r; at higher values of s, widening the portfolio of storage technologies, including options with a higher round-trip efficiency, helps in achieving zero CO_2 emissions; at very high values of s, the storage capacity is not limiting anymore. Furthermore, installing batteries alongside the H_2 storage allows reducing the renewable energy requirement, hence the system cost, due to a more efficient offset of the short-term mismatch between RES generation and energy demand. Considering an average current costs of Li-ion batteries of 200 EUR/kWh [81], and moving along the new zero-emissions curve, we obtain: (i) 310 EUR/MWh for $r = 3, s = 0.05$, (ii) 300 EUR/MWh for $r = 1.7, s = 0.5$, and (iii) 280 EUR/MWh for $r = 1.6, s = 1$.

Finally, we note that the cost of battery storage does not significantly affect the results of the optimization (variations smaller than 10% when halving the battery cost). This is because we perform a minimum-CO_2 emissions optimization, which corresponds to minimizing the amount of lost energy (i.e. minimizing the amount of energy imported from the grid), independently of the cost of system. A higher share of battery storage, as well as a greater impact of the battery cost, would be observed in cost-optimal solutions.

6. Summary of main results and concluding remarks

6.1. Summary

This paper presents a framework to model underground hydrogen storage, which allows to evaluate the potential of salt caverns to reduce CO_2 emissions of renewables-based multi-energy systems (MES). A first-principle model is developed, which accounts for the transport phenomena across the underground rock, and allows describing the dynamics of the stored energy when injecting and withdrawing hydrogen. Then, as such a nonlinear model is intractable for use in the optimization of integrated systems, a linear reduced order model is determined, which is able to accurately describe the storage dynamics under realistic operating conditions. Such a linear model is included within a mixed integer linear program (MILP) optimization framework that determines the optimal design and operation, in terms of minimum CO_2 emissions, of a MES that satisfies the energy demand of a given end-user.

The linear model developed in this work proved to accurately predict the results computed by a detailed model of underground H_2 storage. When modeling H_2 storage in a salt cavern, little to no influence of H_2 diffusion into the rock domain is observed with the detailed model. Accordingly, when underground H_2 storage in salt caverns is investigated via MILP optimization, the flux through the cavern wall can be neglected, resulting in a simple H_2 tank model, yet allowing for considering the set of constraints required to enforce safe structural operation.

The aforementioned optimization framework is implemented to assess the potential of hydrogen storage in reducing the CO_2 emissions of different energy systems featuring different renewable technologies, energy demands, and emission factors of the electricity grid. Such systems are evaluated by introducing two parameters, namely the available renewable energy sources (RES) generation, r, and the available storage capacity, s. The CO_2 emissions of the energy system are then evaluated on the (r,s) plane, where zero-emission regions are defined and assessed with reference to current and future policy scenarios.

Results show that the shape of the CO_2 emissions regions is such that

it is not possible to decrease r and s at the same time while also keeping the emissions at a constant value. Furthermore, for a H_2-based system, for reasonable values of r and s, zero-CO_2 emissions can be obtained only when the RES generation and the energy demand have the same seasonal dynamics, i.e. they peak at the same time of the year. Similarly, H_2 storage makes a seasonal profile of renewable generation, e.g. solar-based generation, much easier to store than a profile characterized by sharp spikes along the year, e.g. wind-based generation. Therefore, lower CO_2 emissions are achieved for the former than for the latter. Combining wind and solar is indeed beneficial for the system because of the different evolution in time of RES availability. On the contrary, the shape of the carbon intensity of the electricity grid has little impact on the MES design and on the resulting CO_2 emissions.

Finally, the combination of short- and long-term storage technologies, namely battery and H_2 cavern, is investigated. Findings show that, for given values of storage capacity and RES generation, the system CO_2 emissions can be reduced by implementing both types of storage to fully exploit the diverse dynamics of the generation-demand mismatch. However, for all r and s values that enable zero CO_2 emissions, the size of H_2 storage is significantly larger than that of the battery, thus highlighting the important role played by large-scale H_2 installations. The H_2 storage is mostly exploited when a high amount of RES and a large storage capacity are available, thus justifying the long-term energy storage, and it is operated in a seasonal fashion only when a high storage capacity is available, as this allows for smooth charging and discharging.

6.2. Concluding remarks

The optimal design of MES with seasonal energy storage is a complex optimization problem due to the types of technology involved and their nonlinear behavior, and to the time variability of the input data. This complexity can be tackled by accounting for all aspects of the optimization problem, which range from the need of reliable models of single technologies to that of computationally-efficient algorithms for optimizing integrated energy systems. Here, we provide a framework that fulfills both such needs by combining an accurate description of H_2 storage in salt caverns with an optimization algorithm able to describe the dynamics of energy generation, storage and consumption. This is enabled by reduced order models that allow capturing the most relevant features of underground H_2 storage while being suited for an MILP optimization framework. This approach enables the analysis of several MES that are characterized by different profiles of renewable generation and energy demand, and untangles the rationale behind the design and operation features determining the pathway towards zero-emission H_2-based energy systems.

Author contribution

Paolo Gabrielli: Conceptualization, Software, Methodology and Formal analysis, Visualization, Writing - Original draft, Editing. **Alessandro Poluzzi**: Resources, Software. **Gert Jan Kramer**: Visualization, Reviewing. **Christopher Spiers**: Methodology, Reviewing. **Marco Mazzotti**: Supervision, Methodology and Formal analysis, Visualization, Reviewing. **Matteo Gazzani**: Supervision, Conceptualization, Methodology and Formal analysis, Visualization, Reviewing, Editing.

Appendix A. Supplementary data

Supplementary data to this article can be found online at https://doi.org/10.1016/j.rser.2019.109629.

References

[1] IPCC. Climate change 2013: the physical science basis. Contribution of working group I to the fifth assessment report of the intergovernmental panel on climate change. Technical report. Cambridge, United Kingdom and New York, NY, USA: IPCC; 2013 [Stocker, T. F., Qin, D., Plattner, G.-K., Tignor, M. M. B., Allen, S. K., Boschung, J., Nauels, A., Xia, Y., Bex, V., Midgley, P. M.], Available at: https://www.ipcc.ch/report/ar5/wg1/.

[2] Child Michael, Otto Koskinen, Linnanen Lassi, Breyer Christian. Sustainability guardrails for energy scenarios of the global energy transition. Renew Sustain Energy Rev 2018;91:321–34.

[3] Susan M. Schoenung. Characteristics and technologies for long- vs. Short-term energy storage. Technical report, sandia national laboratories (SNL), Albuquerque, NM, and Livermore, CA (United States). Available at: http://www.osti.gov/servlets/purl/780306/.

[4] Lund Peter D, Lindgren Juuso, Mikkola Jani, Salpakari Jyri. Review of energy system flexibility measures to enable high levels of variable renewable electricity. Renew Sustain Energy Rev 2015;45:785–807.

[5] Hansen Kenneth, Breyer Christian, Lund Henrik. Status and perspectives on 100% renewable energy systems. Energy 2019;175:471–80.

[6] Pellow Matthew A, Emmott Christopher JM, Barnhart Charles J, Benson Sally M. Hydrogen or batteries for grid storage? A net energy analysis. Energy Environ Sci 2015;8(7):1938–52.

[7] Gabrielli Paolo, Gazzani Matteo, Martelli Emanuele, Mazzotti Marco. Optimal design of multi-energy systems with seasonal storage. Appl Energy 2018;219:408–24.

[8] Malhotra Abhishek, Battke Benedikt, Martin Beuse, Stephan Annegret, Schmidt Tobias. Use cases for stationary battery technologies: a review of the literature and existing projects. Renew Sustain Energy Rev 2016;56:705–21.

[9] Melissa C. Lott and Sang-Il Kim. Technology roadmap: energy storage. Technical report. International Energy Agency; 2014. Available at: http://www.iea.org/publications/freepublications/publication/TechnologyRoadmapEnergystorage.pdf.

[10] Ueckerdt Falko, Pietzcker Robert, Scholz Yvonne, Stetter Daniel, Giannousakis Anastasis, Luderer Gunnar. Decarbonizing global power supply under region-specific consideration of challenges and options of integrating variable renewables in the REMIND model. Energy Econ 2017;64:665–84.

[11] Gregory DP, Ng DYC, Long GM. The hydrogen economy. In: Electrochemistry of cleaner environments. Boston, MA: Springer US; 1972. p. 226–80.

[12] J Kippenhan C, Corlett RC. No Title. In: Hydrogen economy miami energy conference. Miami Beach: Plenum Press; 1975. p. 933–47.

[13] Walters AB. Technical and environmental aspects of underground hydrogen storage. In: World hydrogen energy conference. vol. 2. Miami Beach: Pergamon Press; 1976. A77–33326 14–44.

[14] Carden PO, Paterson Lincoln. Physical, chemical and energy aspects of underground hydrogen storage. Int J Hydrogen Energy 1979;4(6):559–69.

[15] Lindblom Ulf E. A conceptual design for compressed hydrogen storage in mined caverns. Int J Hydrogen Energy 1985;10(10):667–75.

[16] Lord Anna S, Kobos Peter H, Borns David J. Geologic storage of hydrogen: scaling up to meet city transportation demands. Int J Hydrogen Energy 2014;39(28):15570–82.

[17] Netherlands Enterprise Agency. The effects of hydrogen injection in natural gas networks for the Dutch underground storages. Technical report. Ministry of Economic Affairs; 2017. Available at: https://www.rvo.nl/sites/default/files/2017/07/TheΩeffectsofhydrogeninjectioninnaturalgasnetworksfortheDutchundergroundstorages.pdf.

[18] Böttcher Norbert, Görke Uwe-Jens, Kolditz Olaf, Nagel Thomas. Thermo-mechanical investigation of salt caverns for short-term hydrogen storage. Environ Earth Sci 2017;76(3):98.

[19] Tarkowski Radoslaw. Perspectives of using the geological subsurface for hydrogen storage in Poland. Int J Hydrogen Energy 2017;42(1):347–55.

[20] Stone Howard BJ, Veldhuis Ivo, Neil Richardson R. Underground hydrogen storage in the UK. Geol Soc, Lond, Spec Publ 2009;313(1):217–26.

[21] Ozarslan Ahmet. Large-scale hydrogen energy storage in salt caverns. Int J Hydrogen Energy 2012;37(19):14265–77.

[22] Le Duigou Alain, Bader Anne-Gaëlle, Lanoix Jean-Christophe, Nadau Lionel. Relevance and costs of large scale underground hydrogen storage in France. Int J Hydrogen Energy 2017;42(36):22987–3003.

[23] Jan Michalski, Ulrich Bünger, Fritz Crotogino, Donadei Sabine, Schneider Gregor-Sönke, Pregger Thomas, Cao Karl-Kiên, Heide Dominik. Hydrogen generation by electrolysis and storage in salt caverns: potentials, economics and systems aspects with regard to the German energy transition. Int J Hydrogen Energy 2017;42(19):13427–43.

[24] Juez-Larré Joaquim, Van Gessel Serge, Dalman Rory, Remmelts Gijs, Groenenberg Remco. Assessment of underground energy storage potential to support the energy transition in The Netherlands. First Break 2019;37(July):57–66.

[25] Peng Dan D, Fowler Michael, Ali Elkamel, Ali Almansoori, Sean B, Walker. Enabling utility-scale electrical energy storage by a power-to-gas energy hub and

[26] Tarkowski Radoslaw. Underground hydrogen storage: characteristics and prospects. Renew Sustain Energy Rev 2019;105(January):86–94.

[27] Reitenbach Viktor, Ganzer Leonhard, Albrecht Daniel, Hagemann Birger. Influence of added hydrogen on underground gas storage: a review of key issues. Environ Earth Sci 2015;73(11):6927–37.

[28] Bai Mingxing, Song Kaoping, Sun Yuxue, He Mengqi, Yang Li, Sun Jianpeng. An overview of hydrogen underground storage technology and prospects in China. J Pet Sci Eng 2014;124:132–6.

[29] Sainz-Garcia Alvaro, Abarca Elena, Rubi V, Grandia Fidel. Assessment of feasible strategies for seasonal underground hydrogen storage in a saline aquifer. Int J Hydrogen Energy 2017;42(26):16657–66.

[30] Pfeiffer WT, al Hagrey SA, Köhn D, Rabbel W, Bauer S. Porous media hydrogen storage at a synthetic, heterogeneous field site: numerical simulation of storage operation and geophysical monitoring. Environ Earth Sci 2016;75(16):1177.

[31] Heinemann N, Booth MG, Haszeldine RS, Wilkinson M, Scafidi J, Edlmann K. Hydrogen storage in porous geological formations – onshore play opportunities in the midland valley (Scotland, UK). Int J Hydrogen Energy 2018;43(45):20861–74.

[32] Hagemann B, Rasoulzadeh M, Panfilov M, Ganzer L, Reitenbach V. Mathematical modeling of unstable transport in underground hydrogen storage. Environ Earth Sci 2015;73(11):6891–8.

[33] Khaledi Kavan, Mahmoudi Elham, Datcheva Maria, Tom Schanz. Stability and serviceability of underground energy storage caverns in rock salt subjected to mechanical cyclic loading. Int J Rock Mech Min Sci 2016;86:115–31.

[34] Iordache Ioan, Schitea Dorin, Gheorghe Adrian V, Iordache Mihaela. Hydrogen underground storage in Romania, potential directions of development, stakeholders and general aspects. Int J Hydrogen Energy 2014;39(21):11071–81.

[35] Brown TW, Bischof-Niemz T, Blok K, Breyer C, Lund H, Mathiesen BV. Response to 'Burden of proof: a comprehensive review of the feasibility of 100% renewable-electricity systems'. Renew Sustain Energy Rev 2018;92:834–47.

[36] Teske Sven, editor. Achieving the paris climate agreement goals. Cham: Springer International Publishing; 2019.

[37] Zappa William, Martin Junginger, van den Broek Machteld. Is a 100% renewable European power system feasible by 2050? Appl Energy 2019;233–234:1027–50.

[38] Child Michael, Kemfert Claudia, Bogdanov Dmitrii, Breyer Christian. Flexible electricity generation, grid exchange and storage for the transition to a 100% renewable energy system in Europe. Renew Energy 2019;139:80–101.

[39] Bogdanov Dmitrii, Farfan Javier, Sadovskaia Kristina, Aghahosseini Arman, Child Michael, Gulagi Ashish, Oyewo Ayobami Solomon, Barbosa Larissa de Souza Noel Simas, Breyer Christian. Radical transformation pathway towards sustainable electricity via evolutionary steps. Nat Commun 2019;10(1):1077.

[40] Heuberger Clara Franziska, Mac Dowell Niall. Real-world challenges with a rapid transition to 100% renewable power systems. Joule 2018;2(3):367–70.

[41] Peach Colin J, Spiers Christopher J. Influence of crystal plastic deformation on dilatancy and permeability development in synthetic salt rock. Tectonophysics 1996;256(1–4):101–28.

[42] Stormont JC. In situ gas permeability measurements to delineate damage in rock salt. Int J Rock Mech Min Sci 1997;34(7):1055–64.

[43] Alkan Hakan. Percolation model for dilatancy-induced permeability of the excavation damaged zone in rock salt. Int J Rock Mech Min Sci 2009;46(4):716–24.

[44] Liu Wei, Muhammad Nawaz, Chen Jie, Spiers CJ, Peach CJ, Jiang Deyi, Li Yinping. Investigation on the permeability characteristics of bedded salt rocks and the tightness of natural gas caverns in such formations. J Nat Gas Sci Eng 2016;35:468–82.

[45] Raju Mandhapati, Kumar Khaitan Siddhartha. Modeling and simulation of compressed air storage in caverns: a case study of the Huntorf plant. Appl Energy 2012;89(1):474–81.

[46] Kushnir R, Dayan A, Ullmann A. Temperature and pressure variations within compressed air energy storage caverns. Int J Heat Mass Transf 2012;55(21–22):5616–30.

[47] Maton Jean-Paul, Zhao Li, Brouwer Jacob. Dynamic modeling of compressed gas energy storage to complement renewable wind power intermittency. Int J Hydrogen Energy 2013;38(19):7867–80.

[48] Vanessa Tietze, Stolten Detlef. Thermodynamics of pressurized gas storage. In: Hydrogen science and engineering : materials, processes, systems and technology. Weinheim, Germany: Wiley-VCH Verlag GmbH & Co. KGaA; 2016. p. 601–28 [chapter 25].

[49] Gillhaus Axel. Natural gas storage in salt caverns - present status, developments and future trends in Europe. Technical report. 2007. Available at: https://pdfs.semanticscholar.org/ab03/bf76c70ea49e297b5673e2455bd67dbfcfdc.pdf?%7b%5f%7dga=2.10787703.2130565779.1566900424-1658795583.1546620914.

[50] Bonté Damien, Diederik van Wees Jan, Verweij JM. Subsurface temperature of the onshore Netherlands: new temperature dataset and modelling. Neth J Geosci 2012;91(04):491–515.

[51] Urai Janos L, Spiers Christopher J, Zwart Hendrik J, Lister Gordon S. Weakening of rock salt by water during long-term creep. Nature 1986;324(6097):554–7.

[52] European Commission. Impact of the excavation disturbed or damaged zone (EDZ) on the performance of radioactive waste geological repositories. Technical report. Directorate - General for Research and Innovation; 2003. Available at: https://publications.europa.eu/en/publication-detail/-/publication/99a07bde-8a5d-49ff-9bb0-23c42949846d.

[53] Waldmann Svenja, Gaupp Reinhard. Grain-rimming kaolinite in Permian Rotliegend reservoir rocks. Sediment Geol 2016;335:17–33.

[54] Klinkenberg LJ. The permeability of porous media to liquids and gases. Technical report. American Petroleum Institute; 1941. Available at: http://proceedings.socar.az/uploads/pdf/11/57-73%7b%5f%7dKlinker.pdf.

[55] Dullien FAL. Porous media - fluid Transport and pore structure. Elsevier Inc.; 1979.

[56] Jones SC. Using the inertial coefficient, B, to characterize heterogeneity in reservoir rock. In: Proceedings of SPE annual technical conference and exhibition. Society of Petroleum Engineers; 1987. p. 165–74. number 2.

[57] Zheng Qian, Yu Boming, Duan Yonggang, Fang Quantang. A fractal model for gas slippage factor in porous media in the slip flow regime. Chem Eng Sci 2013;87:209–15.

[58] LeVeque RJ. Finite volume methods for hyperbolic problems. Cambridge University Press; 2002.

[59] Landinger Hubert, Ulrich Bünger, Raksha Tetyana, Jesus Simon, Correas Luis. Benchmarking of large scale hydrogen underground storage. Technical report. European Union; 2013. Available at: http://hyunder.eu/wp-content/uploads/2016/01/D2.1_Benchmarking-of-large-scale-seasonal-hydrogen-underground-storage-with-competing-options.pdf.

[60] Kruck Olaf, Fritz Crotogino. Assessment of the potential, the actors and relevant business cases for large scale and seasonal storage of renewable electricity by hydrogen underground storage in Europe: benchmarking of selected storage options. 2013. Available at: http://hyunder.eu/wp-content/uploads/2016/01/D3.3%7b%5f%7dBenchmarking-of-selected-storage-options.pdf.

[61] Wu Yu-Shu, Pruess Karsten, peter Persoff. Gas flow in porous media with klinkenberg effects. Transp Porous Media Jul 1998;32(1):117–37.

[62] Mancarella Pierluigi. MES (multi-energy systems): an overview of concepts and evaluation models. Energy 2014;65:1–17.

[63] Daniel Quiggin, Buswell Richard. The implications of heat electrification on national electrical supply-demand balance under published 2050 energy scenarios. Energy 2016;98:253–70.

[64] Heinen Steve, Turner William, Cradden Lucy, McDermott Frank, O'Malley Mark. Electrification of residential space heating considering coincidental weather events and building thermal inertia: a system-wide planning analysis. Energy 2017;127:136–54.

[65] Gabrielli Paolo, Fürer Florian, Mavromatidis Georgios, Mazzotti Marco. Robust and optimal design of multi-energy systems with seasonal storage through uncertainty analysis. Appl Energy 2019;238:1192–210.

[66] Eurostat. Share of renewable energy in gross final energy consumption. Available at. 2019. Accessed on 2019-09-04, https://ec.europa.eu/eurostat/tgm/table.do?tab=table&init=1&language=en&pcode=t2020_31&plugin=1.

[67] Statista. Pumped hydropower storage capacity of selected European countries in 2018. 2019. Accessed on 2019-09-04, https://www.statista.com/statistics/690032/pumped-storage-capacity-europe/.

[68] Gabrielli Paolo, Gazzani Matteo, Mazzotti Marco. Electrochemical conversion technologies for optimal design of decentralized multi-energy systems : modeling framework and technology assessment. Appl Energy 2018;221:557–75.

[69] AspenPlus V8. 2014;6.

[70] Gabrielli Paolo, Flamm Ben, Eichler Annika, Gazzani Matteo, Lygeros John, Mazzotti Marco. Modeling for optimal operation of PEM fuel cells and electrolyzers. In: 2016 IEEE 16th international conference on environment and electrical engineering (EEEIC). vols. 1–7. IEEE; 2016.

[71] Ehrgott Matthias. Multicriteria optimization. Springer; 2005.

[72] Chevrier Alice. Calculation of a dynamic carbon factor for the Swiss electricity grid. Semester thesis. ETH Zurich; 2016.

[73] Artelys. Effect of high shares of renewables on power systems. Technical report. Bruxelles: European Commission; 2018. Available at: https://publications.europa.eu/en/publication-detail/-/publication/01c456f4-7144-11e9-9f05-01aa75ed71a1/language-en/format-PDF/source-96288175.

[74] EU EU. Reference scenario 2016. 2018. Accessed on 2019-08-27, https://ec.europa.eu/energy/en/data-analysis/energy-modelling/eu-reference-scenario-2016.

[75] Shell Sky Scenario. The numbers behind Sky. 2019. Accessed on 2019-08-27, https://www.shell.com/energy-and-innovation/the-energy-future/scenarios/shell-scenario-sky.html.

[76] IEA Technology. Roadmap: hydrogen and fuel cells technical assessment. Technical report. International Energy Agency; 2015. Available at: http://ieahydrogen.org/pdfs/TechnologyRoadmapHydrogenandFuelCells-(1).aspx.

[77] Pleßmann G, Blechinger P. How to meet EU GHG emission reduction targets? A model based decarbonization pathway for Europe's electricity supply system until 2050. Energy Strategy Rev 2017;15:19–32.

[78] Christian Gils Hans, Scholz Yvonne, Pregger Thomas, de Tena Diego Luca, Heide Dominik. Integrated modelling of variable renewable energy-based power supply in Europe. Energy 2017;123:173–88.

[79] Bussar Christian, Stöcker Philipp, Cai Zhuang, Moraes Jr Luiz. Dirk magnor, pablo Wiernes, Niklas van Bracht, Albert moser, and Dirk Uwe Sauer. Large-scale integration of renewable energies and impact on storage demand in a European renewable power system of 2050–sensitivity study. J Energy Storage 2016;6(1–10).

[80] Siemens. Hydrogen solutions. 2019. Accessed on 2019-08-27, https://new.siemens.com/global/en/products/energy/renewable-energy/hydrogen-solutions.html.

[81] BloombergNEF A. Behind the scenes take on lithium-ion battery prices. 2019. Accessed on 2019-08-27, https://about.bnef.com/blog/behind-scenes-take-lithium-ion-battery-prices/.